J. Fluid Mech. (1996), *vol.* 323, *pp.* 23–63

Scalar mixing and reaction in plane liquid shear layers

By P. S. KARASSO AND M. G. MUNGAL
Mechanical Engineering Department, Stanford University, Stanford, California 94305-3032, USA

(Received 12 July 1994 and in revised form 22 April 1996)

The scalar (concentration) field of two-dimensional liquid mixing layers was investigated at post-mixing-transition conditions. The planar laser-induced fluorescence technique was used for passive scalar measurements, and for chemical product measurements. Following the approach of Koochesfahani & Dimotakis (1986), the chemical product results were used to make resolution-free estimates of mixed-fluid quantities, thus providing a check on the accuracy of the passive scalar measurements. The operating conditions were systematically varied to study the effect of various parameters (Reynolds number, speed ratio, and initial boundary-layer momentum thickness) on the structure of the layer. At conditions which are just past the mixing transition, the study essentially duplicated the results obtained by Koochesfahani & Dimotakis: the chemical-product concentration profiles at high- and low-stoichiometric ratios (flip experiments) were symmetric and the average concentration of mixed-fluid was uniform across the layer. However, when the layer was pushed to more fully developed conditions, its scalar field evolved to an asymptotic state: the two flip chemical-product concentration profiles developed modest asymmetries, and the average mixed-fluid concentration developed a small variation across the layer, but the change was less than that observed in gases. Based on the chemical reaction data, we infer that the mixture fraction probability density function (p.d.f.) for the fully-developed liquid layer evolves from a 'non-marching' type to a 'tilted' type. Despite the observed evolution, the average mixed-fluid concentration remained fixed for all the layers past the mixing transition, while the total mixed-fluid probability (the total amount of mixed fluid normalized by the layer's width) showed only a very slight increasing tendency as the layer reached fully developed conditions. The mixture fraction p.d.f., measured by the passive scalar approach, is shown and discussed for a broad range of cases. While it overpredicts the amount of mixing, it showed a qualitatively-correct 'non-marching' character initially, but evolved to a qualitatively-incorrect 'marching' character at the asymptotic state. The reasons for the poor estimation of the p.d.f. by the passive scalar approach, at fully developed conditions, are attributed to changes in the flow and lack of resolution and suggests caution when using such measures. Furthermore, the study also showed that the Reynolds number alone is inadequate to characterize the state of the layer. A different parameter (the 'pairing parameter'), which accounts for the initial boundary layers and scales with the number of vortex mergings, was found to better explain the evolution in the structure of the scalar field.

1. Introduction

Shear layers represent an important class of flows for the study of scalar mixing by turbulence. From a technological point of view, measuring the total amount of mixed fluid, and understanding the limitations imposed by the flow under consideration, is crucial for the performance of many systems. Such systems include combustion and propulsion devices, chemical processing and environmental applications. From a theoretical point of view, the plane shear layer offers a model flow (quasi two-dimensional, constant boundary conditions and self-preservation) to study the development of instability modes, the turbulence cascade, and the difference between momentum mixing and scalar mixing. Furthermore, the study of molecularly-mixed fluid provides a direct picture of the state of the smallest scales encountered in turbulence.

The study of shear-layer flows increased after the discovery by Brown & Roshko (1974) of spanwise large-scale structures that dominate the mixing layer throughout its fully developed regime. These structures were attributed to the Kelvin–Helmholtz (K–H) instability mode, which is now considered to be the primary instability mode in shear layers. Others investigators (Winant & Browand 1974; Dimotakis & Brown 1976; Browand & Troutt 1980) confirmed the existence of these structures at high Reynolds numbers, and showed that pairings and tearings among them contribute significantly to the layer's development; similar evidence at very high Reynolds numbers was provided by Clemens & Mungal (1992, 1995). A secondary instability mode associated with streamwise vortical structures, was also observed in plane shear layers (Konrad 1976; Breidenthal 1978). The spanwise and the streamwise vortex structures were found to occur simultaneously (Bernal & Roshko 1986; Jimenez, Cogollos & Bernal 1985; Karasso & Mungal 1990) with the streamwise vortices being arranged in counter-rotating vortex pairs.

The study of scalar mixing from a large-scale-structure point of view is important since, according to many investigators, the entrainment of free-stream fluid (and hence the growth rate) and the composition field of the layer are controlled by the large-scale-structure dynamics. Huang & Ho (1990) found that the generation and transition to the small turbulent eddies occurs through vortex pairings. They showed that the transition to the fully developed regime correlates with the number of pairings of the large-scale vortices, which in turn depends on the operating conditions (speed ratio, velocity magnitudes) and the downstream location. Their findings have important implications for the present study, since it is the small scales that ultimately effect the scalar mixing. Furthermore, Bradshaw (1966) showed that the development of the mixing layer is greatly affected by the state of its initial boundary layers. Finally, there are a number of studies (Hussain & Clark 1981; Wood & Bradshaw 1982) which view the large-scale structures as a result of forcing or as a relic of transition, rather than as an integral part of the turbulence.

Scalar mixing is often measured quantitatively by probing the flow's local concentration of either a passive scalar (e.g. a dye uniformly seeded into one of the free streams), or of a chemical product which is formed as a result of mixing and reaction between the fluids carried by the two free streams. It is well known that the resolution of the measurements severely affects the character of the results. We define:

$$\text{relative resolution} \equiv \frac{L}{\lambda_B}.$$

Here L is the measuring probe's largest dimension, where L takes into account the

probe's size and its time response (converted to spatial dimension by multiplying with the flow's local mean velocity); λ_B is the mass diffusion scale (Batchelor's scale), which represents the smallest physical lengthscale for mixing. Breidenthal (1981) and Koochesfahani & Dimotakis (1986) showed that passive scalar measurements with a probe of $L/\lambda_B > 1$, will yield an incorrect (overpredicted) amount of mixed fluid, as the probe cannot distinguish mixed fluid from stirred fluid. The Batchelor scale, which can be approximated by:

$$\lambda_B \approx \delta Re^{-0.75} Sc^{-0.5} \tag{1}$$

(δ is the average visual thickness, Re is the Reynolds number based on visual thickness and free-stream velocity difference, and Sc is the Schmidt number), sets very stringent requirements on the size of the probe. The situation is much worse in liquids where the Schmidt number is three orders of magnitude larger than in gases. A typical value of λ_B for a water flow at $Re \approx 30000$ is $\lambda_B \approx 1$ μm. To overcome resolution limitations, a chemical-reaction technique has been employed to monitor mixing (Breidenthal 1981; Mungal & Dimotakis 1984; Koochesfahani & Dimotakis 1986). In this technique, the entrained free-stream fluids carry reactants, and the chemical product which is formed is measured. This technique still does not yield spatially resolved measurements since the probe is larger than the Batchelor scale, but the average amount of chemical product within the sampled volume is correct. In the limit of a fast chemical reaction ($Da \gg 1$, where Da is the Damköhler number, defined as the ratio of the mixing timescale to the chemical-reaction timescale) which does not alter the flow-field characteristics, the chemical product can be related to the mixed fluid (Koochesfahani & Dimotakis 1986).

An often used, compact representation of the composition field in the layer is the probability density function (p.d.f.) of the mixture fraction. The mixture fraction, ξ, is defined as the fraction of high-speed fluid in the mixture within the sampled volume ($\xi = 1$ corresponds to pure high-speed stream fluid, $\xi = 0$ corresponds to pure low-speed stream fluid) and can be thought of synonymously with concentration, C, for uniform density flows. The issues related to the p.d.f. play a central role in this paper. Therefore, it is useful at this point to introduce several idealized p.d.f.-shapes (figure 1) which will provide a framework for the discussion to follow. Figure 1 (*a*) shows a 'non-marching' p.d.f., where the most probable value of the mixture fraction of mixed fluid (shown as a delta function) is invariant across the normalized width (y/δ) of the layer. Figure 1 (*b*) shows the idealized form of a 'marching' p.d.f., for which the most probable mixture-fraction value of mixed fluid is the average mixture fraction at a given location across the layer. Finally, figure 1 (*c*) shows a p.d.f. with a behaviour intermediate to marching and non-marching, and which hereinafter is termed 'tilted'. The curves shown with dotted lines will be discussed later.

Using passive scalar measurements, Konrad (1976) and Koochesfahani & Dimotakis (1986) measured the p.d.f. in a mixing layer at $Re = 32000$ (gas) and $Re = 23000$ (liquid), respectively. Their results showed a non-marching p.d.f., with the preferred mixture fraction corresponding to the entrainment ratio. The range of Reynolds numbers quoted above is considered to be moderate and just beyond the mixing transition. The shape of these p.d.f.s in connection to the observed K–H large-scale structures, suggested that it is the dynamics of the large-scale structures that control the composition field. An additional, important conclusion of these studies was that the shear layer does not entrain equal amounts of fluid from each of the two free streams, and that free-stream fluid could be transported across the layer by the large-scale motions but remain unmixed. In sharp contrast with the above, are the measurements

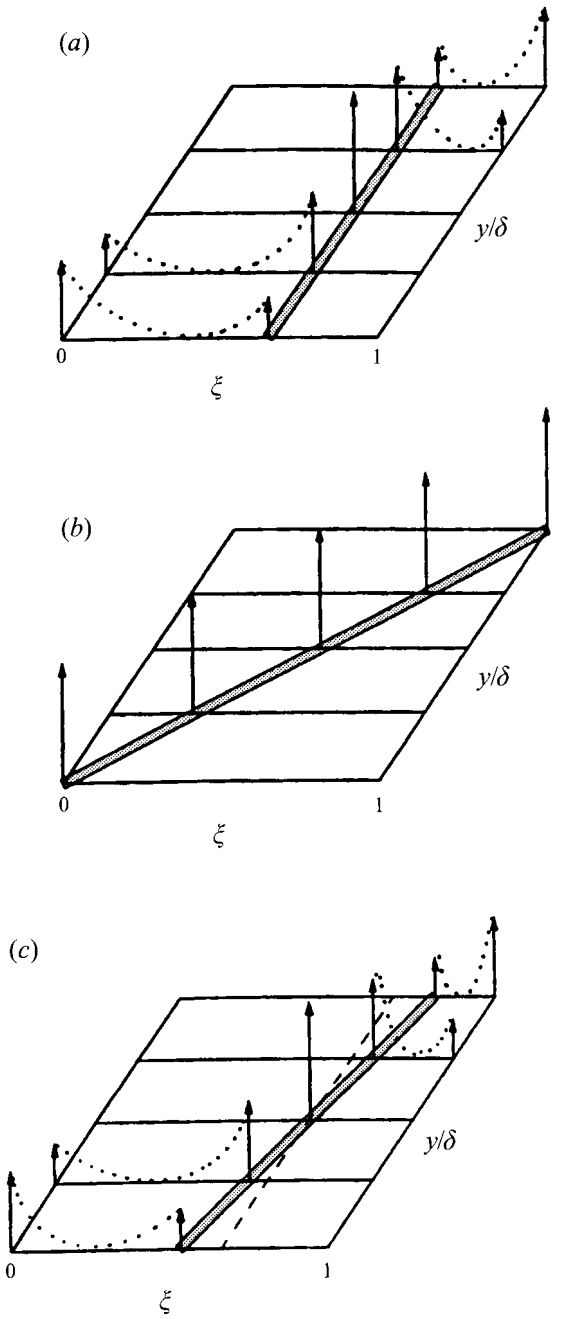

FIGURE 1. Idealized p.d.f.s (*a*) 'non-marching' type, (*b*) 'marching' type, (*c*) 'tilted' type. ——, liquid; · · ·, gas.

by Batt (1977) in a gaseous mixing layer at $Re = 70000$, which showed a p.d.f. which is marching, with no unmixed fluid within the layer.

Breidenthal (1981) performed experiments in a liquid (water) layer using a chemical-reaction technique. Comparison of his results with those from Konrad showed that the amount of chemical product formed in a liquid layer was about $\frac{3}{4}$ that in a gaseous layer (Breidenthal's data is now believed to have errors, owing to miscalibrations in his technique, see Koochesfahani 1984). The difference was attributed to Schmidt number

effects ($Sc \approx 1$ in gases, and ≈ 2000 for the water/dye system). Broadwell & Breidenthal (1982), taking into account these results and the large-scale-structure visualizations, developed a model for turbulent mixing. In this model, an explicit dependence of the amount of mixed fluid on the Reynolds number and on the Schmidt number is proposed. The model predicted different amounts of chemical product for gases and for liquids, at increasing Reynolds numbers. Dimotakis (1989) has also developed a model based on the large-scale motion which captures the differences between gases and liquids, but has a different high-Reynolds-number dependence.

Mungal & Dimotakis (1984) measured the chemical product in a gas-phase mixing layer at $Re = 65000$. By performing pairs of 'flip' experiments (where the same reactants are exchanged between the high- and low-speed side) at various stoichiometric ratios (ϕ), they showed that the layer entrains asymmetrically from each free stream, and it matters whether the lean reactant is placed on the high- or on the low-speed side. In a follow-up work to examine the effects of Reynolds number (Mungal, Hermanson & Dimotakis 1985), it was shown that the amount of chemical product (gaseous layers) decreases as the Reynolds number increases; similar results were subsequently reported by Frieler (1992). Frieler also inverted his chemical-reaction data and mathematically constructed the mixture fraction p.d.f. His p.d.f. was non-marching for $Re = 15000$, but at higher Reynolds numbers ($Re = 36000$ and $Re = 62000$) the p.d.f. evolved to become tilted (of the type sketched in figure 1*c*).

Koochesfahani & Dimotakis (1986, hereinafter referred to as KD) measured a liquid chemically-reacting layer at $Re = 23000$, and showed that both the amount and the composition of mixed fluid differs significantly (a factor of 2) between gases and liquids. They confirmed that the layer entrains free-stream fluid asymmetrically, and demonstrated the severe resolution limitations of passive scalar measurements. They also revised Breidenthal's estimates to show that $\approx 50\%$ less chemical product is formed in liquids than in gases: in the context of the Broadwell–Breidenthal model, this was interpreted as the effect of high Sc resulting in a negligible amount of product residing in the strained laminar sheets.

The available gaseous-phase data suggest less efficient mixing as Re increases, accompanied by a change in the composition field (as shown by Frieler's p.d.f.s). For liquid layers, the matter is less clear owing to lack of data. The only (post-mixing-transition) accurate data-point is provided by KD for $Re = 23000$. KD performed an additional high-ϕ measurement at $Re \approx 78000$ and found that the normalized amount of chemical product remained unchanged. This result led them to the conclusion that the behaviour measured at $Re = 23000$ represented the asymptotic state of liquid layers. Obviously, such an assertion needs more data to be proven, and constitutes one of the objectives of the present work. Frieler has demonstrated that inferring the amount of mixed fluid from reacting experiments at a single ϕ can lead to wrong conclusions. On the other hand, mixing in gases and liquids is different, and so one cannot extrapolate results from one phase to the other.

As mentioned before, passive scalar measurements are unreliable owing to resolution requirements. The non-marching p.d.f. obtained by Konrad is believed to be qualitatively correct, based on reasonably well-resolved data ($L/\lambda_B \approx 20/1$) (see comparisons in Mungal & Dimotakis 1984). Hence, Batt's marching p.d.f. could be attributed to the lower resolution of his measurements ($L/\lambda_B \approx 60/1$). Both of these results pertain to experiments in gas phase, with a Schmidt number of the order of 1. Resolution alone cannot explain the above variance in the shape of the p.d.f.: KD obtained a non-marching p.d.f. in a liquid layer with $L/\lambda_B \approx 1200/1$, which is an order of magnitude worse than Batt's. On the other hand, Frieler's resolution-free p.d.f. (for

gaseous layers) was of non-marching type at $Re = 15000$, but at $Re = 62000$ showed a tilted behaviour. It thus appears that, at least for gaseous-phase layers, the p.d.f. evolves with Reynolds number. In conjunction with Frieler's results, it seems that Batt's p.d.f. is not merely the result of poor resolution, but may also reflect an evolution of the mixing field relative to Konrad. Again, pertinent liquid-layer data at high Reynolds numbers do not exist. Thus, a further objective of the present work will be to reconcile all the various p.d.f.'s measured to date.

A better understanding of scalar mixing requires more experiments for liquid-phase layers at high Reynolds numbers; the present work will attempt to provide these. We perform detailed mixing measurements (passive scalar and chemical reaction) in liquid turbulent mixing layers at different operating conditions (speed ratio, velocity magnitudes). All layers are examined at conditions past the mixing transition. By changing the operating conditions of layers with similar Re, the effect of initial conditions (initial boundary-layer momentum thickness) on the structure of the layer is assessed. The most important results of this work are the chemical-reaction experiments which are used to (i) directly measure the amount of chemical product formed in the layer at different flow regimes, (ii) to make resolution-free estimates of mixed-fluid properties in the layer, and (iii) to reconcile past and present measurements of the passive scalar p.d.f. Important quantities we wish to determine are the mixture fraction p.d.f., the distribution of mixed fluid and of chemical product, the entrainment ratio and the growth rate. The measurements' resolution is thoroughly addressed by comparing the passive-scalar with the chemical-product measurements. To further investigate the effect of initial conditions on the scalar field, the boundary layer on the high-speed side of the splitter plane is tripped for selected cases.

The results shown below will be presented as follows: §2 describes the experimental facility and experimental approach used. Section 3 shows visualizations of the layer to ensure that the layer is essentially normally behaved. Section 4 presents chemical reaction results to establish resolution-free estimates of mixing efficiency. Section 5 presents detailed passive scalar measurements and p.d.f.s for comparison to the chemically reacting results. Section 6 presents detailed comparisons among the present measurements and previous work and conclusions are given in §7.

2. Experimental details

2.1. *Facility*

A schematic of the facility (and the experimental arrangement) is shown in figure 2. It consists of a blow-down water tunnel which is made entirely out of Plexiglas. The overhead tank is partitioned, thus creating two independent feeding plenums for the two streams of the mixing layer. The velocity magnitudes of the two streams are controlled independently by air-admittance valves. These valves also defeat the unsteady Bernoulli term that arises from the falling head as the tanks drain during the run. The available run-times range from 30 s to 2 min, depending on the speeds that are chosen. A set of honeycomb and screens is placed just prior to the nozzle that leads to the test section. The test section consists of straight sidewalls and endwalls and has a size of 16 cm (span), by 10 cm (width), by 40 cm (length). The splitter plate is positioned asymmetrically to account for the known shift of the shear layer towards the low-speed stream, with the splitter plate tip being at 6 cm from the low-speed sidewall and at 4 cm from the high-speed sidewall. The facility can be operated at various speed ratios between the two streams. For reference, we shall denote by x the streamwise direction, y the cross-stream direction (layer thickness), and z the spanwise direction.

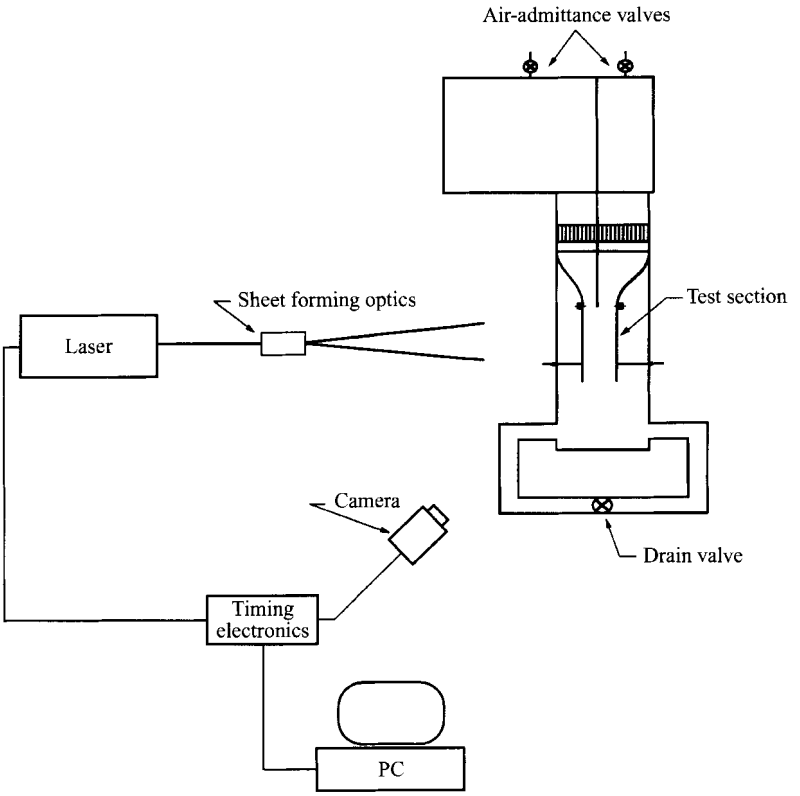

FIGURE 2. Schematic of the flow facility and experimental set-up.

2.2. *The planar LIF technique*

The planar laser-induced fluorescence technique (PLIF) is used to acquire quantitative images of the concentration field across the layer. Details on the theory and implementation of PLIF can be found in various references (Kychakoff, Howe & Hanson 1984; Koochesfahani 1984; Hanson 1986). Very briefly, laser-induced fluorescence signals can be related to concentration of fluorescent species in the flow, and to mixing between two fluid streams if the fluorescent molecules are supplied by only one of the streams. Since fluorescence emission is diffuse, the signals can be imaged and represent point-resolved measurements of the flow field. For our experiment, where the temperature, the density and the pressure are constant, the interpretation of the signal depends primarily on: (*a*) determining the laser-light intensity at each point in the flow through monitoring the spatial intensity distribution of the light sheet, and through light-absorption calculations; (*b*) ensuring a given response (usually linear) on the fluorescence signal with laser light energy and with concentration of the fluorescent species. The PLIF techniques was used in this work for passive scalar measurements, and chemical product measurements. Koochesfahani (1984), who first performed similar experiments in the aqueous phase, discusses details on the LIF technique. In the present work, however, different lasers (and fluorescent tracers) were used, rendering careful calibration imperative. In what follows we give a brief description for each technique, with full details available in Karasso (1994).

2.2.1. *Passive scalar measurements*

Here, a fluorescent dye is uniformly seeded into one of the free-stream reservoirs (the low-speed side), whereas the other stream remains pure water. A thin light sheet oriented in the (x, y)-plane is generated from a laser. Two different laser/fluorescent dye systems are used. The first system, used in most of the cases, consists of a pulsed 20 W copper-vapour laser (CVL) (at the 510.6 nm line), with sodium fluorescein as the tracer diluted to a 2.9×10^{-6} M concentration in the feeding reservoir. For this laser, the light sheet thickness is about 750 μm at the focusing plane, and is formed with appropriate optics (using a long focal length lens arrangement in order to minimize the waist variation of the Gaussian beam), a dichroic beam-splitter (to separate the 578.3 nm line of the CVL), and a pinhole arrangement to reject the more rapidly angularly diverging modes in order to achieve better focusing (which results in the rejection of a fraction of the laser's output energy). The second system consists of a 1.5 W Nd:YAG laser (light-sheet thickness < 500 μm), and the low-speed stream seeded with 5(&6)-carboxy 2′7′-dichlorofluorescein dye to a 1.5×10^{-6} M concentration. The characteristics of this second system, and the choice of the fluorescent tracer in particular, are described in detail in Karasso & Mungal (1996). A two-dimensional CCD array (Cohu 6510 interlaced camera) is used to record the fluorescence signals for all cases. The array is checked for linearity of response, and its fixed-gain pattern is taken into account during image processing. The camera collects the light at a right angle with respect to the laser sheet. Appropriate filters are placed on front of the camera lens to reject scattered light at the laser's line wavelength. In each case, the laser is triggered with pulses that are synchronized with the camera's internal electronic signals, to ensure a single laser pulse during each frame's integration time. The images are acquired and digitized to 512×240 pixels, using a 8-bit frame grabber (Data Translation DT-2151) and a PC-compatible computer. For reasons explained in the following section, we ensured that the water was at a uniform pH of nine or above.

Linearity tests of fluorescence signal *vs.* dye concentration were performed for both fluorescent dyes; the response was linear for the range of dye concentrations used in this experiment. Furthermore, the Lambert–Beer absorption law was checked using a static cell (i.e. a calibration cell made out of Plexiglas) filled with a dye solution of uniform concentration. The validity and consistency of the Lambert–Beer law were verified under different laser energies. The above implied that no fluorescence trapping (i.e. reabsorption of emitted fluorescence within the flow) or photobleaching would occur in the flowing system. Following these tests, each image could be reliably processed to concentration.

Finally, a number of measurements were carried out using both laser systems under the same experimental conditions, and identical results were obtained, reinforcing the belief that the experimental technique is correct.

2.2.2. *Chemical product measurements*

The chemical reaction used is similar to that employed by KD. The implementation involves a fast reaction of the type $A + B \rightarrow P$, where reactant A (H_2SO_4 acid solution, pH ≈ 3) is diluted into one free stream and reactant B (NaOH base solution, pH ≈ 12.3) into the other free stream. The acid–base reaction between the two free-stream fluids is used to 'turn on' the fluorescence of a pH-sensitive dye (sodium fluorescein). The flow is again illuminated with a light sheet from the CVL. The dye is uniformly diluted into the free-stream carrying the acid solution; in this low pH environment, fluorescence is suppressed. Upon excitation, the dye molecules fluoresce

only when the local pH is higher than a certain threshold value: the local pH can only be raised as a result of true molecular mixing (and not stirring) between the two free streams. The fluorescence 'turn on' is virtually a step function on the mixture fraction scale. The emitted fluorescence represents the product P, which is measured (imaged on the camera) to provide an instantaneous distribution of chemical-product concentration across the layer. A static cell is used to monitor the laser sheet distribution and the maximum reference signal.

The stoichiometric ratio of the reaction, ϕ, is defined as the parts of high-speed fluid needed to titrate (i.e. raise the pH to a level where the dye fluorescence is 'turned on') one part of low-speed fluid. The strength of the acid and base solutions were chosen so that the fluorescence 'turn on' would occur when one part of base solution (first free stream) mixed with approximately 16 parts of acid solution (second free stream). Following the technique of Mungal & Dimotakis (1984) and of KD, a pair of 'flip' experiments were run for each case-layer, where the two reactants were exchanged between the high- and the low-speed side. Thus, each layer was measured at both $\phi = 16/1$, and $\phi = 1/16$: these two runs are taken as representatives of runs with $\phi \to \infty$ and $\phi \to 0$, respectively. As was shown by KD, the flip runs provide the basis for making resolution-free estimates of *mixed-fluid* quantities. By implementing a reaction with $\phi \to 0$ and $\phi \to \infty$, the lean reactant (which is locally consumed) is exchanged between the high- and low-speed side, and the measured average chemical product becomes essentially a marker of the entrained free-stream fluid that carries the lean reactant.

2.3. *Experimental conditions*

A first set of experiments was performed at a speed ratio $r = U_2/U_1 = \frac{1}{4}$ (subscripts 1 and 2 denote the high- and the low-speed side, respectively). Three different cases were examined, corresponding to high-speed-stream velocity magnitudes, U_1, of 0.34 m s^{-1}, 0.95 m s^{-1}, and 1.90 m s^{-1}. All cases are summarized in table 1 (other entries in this table will be explained as the discussion proceeds). A second set of experiments was performed at a speed ratio $r = 1/2.65$ (matching the speed ratio of Konrad, Frieler and of KD), for $U_1 = 0.70$ m s^{-1} and $U_1 = 1.05$ m s^{-1}. The camera's field of view was centred to the area $x \approx 25$ cm downstream of the splitter plate. The imaged region during the passive scalar experiments was approximately 7.2 cm (in the cross-stream direction) by 5.4 cm (in the streamwise direction), while for the chemical-reaction experiments it was somewhat larger, 9.7×7.2 cm^2. The boundary-layer momentum thickness θ at the splitter-plate tip was estimated for each case using Thwaites' method, and is shown in table 1. Finally, a trip-wire (1.6 mm in diameter) was placed on the splitter plate at the high-speed side, in order to cause the boundary layer to become turbulent; the trip-wire was positioned 6 cm upstream of the splitter-plate tip (hereinafter, experiments where the trip-wire was used will be termed as 'tripped', while the others as 'untripped'.) Selected cases from the untripped layers were examined under tripped boundary-layer conditions (see table 1). The location and field of view of the camera were the same as before for all cases. For each case, about 100 images were acquired and used for the statistical analysis.

As a way of verifying good experimental conditions and of excluding the possibility of any artificial excitation by the facility on the layer, qualitative panoramic views of the mixing layer were obtained for selective cases. These pictures also aid in gaining insight into the structure of the laser, whereas their average provides information on the shear-layer growth. The panoramic pictures were also obtained through PLIF by enlarging the camera's field of view.

	Laser system	Speed ratio	U_1 (m s^{-1})	Initial boundary-layer conditions	δ (cm) at $x = 25$ cm	Re	λ_B (μm)	L/λ_B	θ (cm)	Pairing parameter	PDF type
Present study	CVL	$\frac{1}{4}$	0.34	Untripped	5.4	14000	0.96	780	0.028	17.8	Non-marching
Present study	Nd:YAG	$\frac{1}{4}$	0.34	Tripped	5.2	13500	—	—	—	—	Non-marching
Present study	CVL	$\frac{1}{4}$	0.95	Untripped	4.8	35000	0.43	1750	0.017	29.5	Marching
Present study	Nd:YAG	$\frac{1}{4}$	0.95	Tripped	3.7	26900	—	—	—	—	Marching
Present study	CVL	$\frac{1}{4}$	1.9	Untripped	4.4	64000	0.25	3000	0.012	42	Marching
Present study	Nd:YAG	$\frac{1}{4}$	1.9	Tripped	3.7	53800	—	—	—	—	Marching
Present study	CVL	$\frac{1}{2.63}$	0.7	Untripped	4.3	18500	0.62	1200	0.020	18.7	Non-marching
Present study	CVL	$\frac{1}{2.63}$	0.7	Tripped	3.1	13700	—	—	—	—	Marching
Present study	CVL	$\frac{1}{2.63}$	1.05	Untripped	4.0	27000	0.43	1750	0.016	23.5	Marching
KD	—	$\frac{1}{2.6}$	0.70	Untripped	—	23000	0.64	1200	0.024	15.6	Non-marching
Konrad	—	$\frac{1}{2.6}$	10.0	Untripped	—	32000	10.5	19	0.007	21.7	Non-marching
Batt	—	0	7.0	Untripped	—	70000	41.6	60	0.046	34	Marching
Frieler	—	$\frac{1}{2.6}$	3.5	Untripped	—	15000	—	—	0.048	14.3	Non-marching*
Frieler	—	$\frac{1}{2.6}$	9.9	Untripped	—	36000	—	—	0.020	23.8	Tilted*
Frieler	—	$\frac{1}{2.6}$	22	Untripped	—	62000	—	—	0.014	36	Tilted*

* Denotes a PDF which was mathematically constructed to fit chemical-reaction data.

TABLE 1. Run conditions, summary of passive scalar results, and comparison with literature data

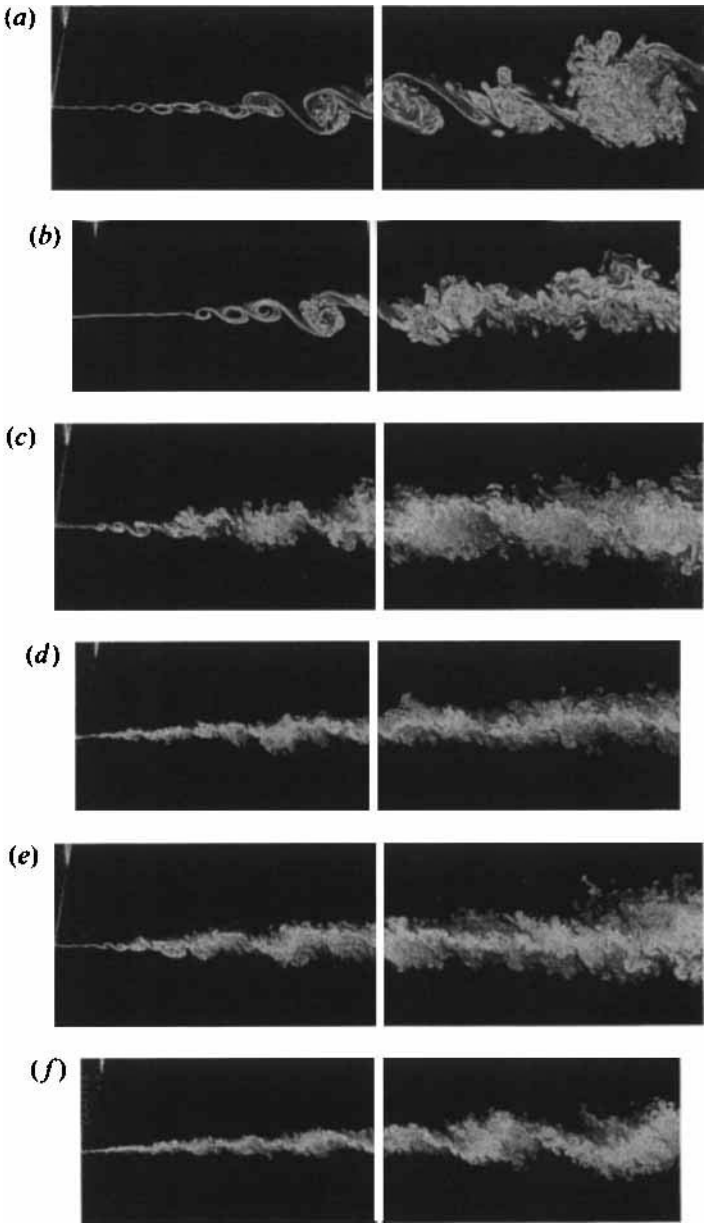

FIGURE 3. Panoramic side views (each composed of two independent images) for $r = \frac{1}{4}$: (*a*) untripped $U_1 = 0.34$ m s^{-1}, (*b*) tripped $U_1 = 0.34$ m s^{-1}, (*c*) untripped $U_1 = 0.95$ m s^{-1}, (*d*) tripped $U_1 = 0.95$ m s^{-1}, (*e*) untripped $U_1 = 1.90$ m s^{-1}, (*f*) tripped $U_1 = 1.90$ m s^{-1}.

3. Visualization results

3.1. *Panoramic side views*

Samples of panoramic views of the layer are presented in figure 3, for the speed ratio of $r = \frac{1}{4}$ and for high-speed stream velocity magnitudes of 0.34 m s^{-1}, 0.95 m s^{-1}, and 1.9 m s^{-1} (untripped and tripped). Flow is from left to right, and the low-speed stream is on the upper side of each image. The views (each composed to two independent realizations) show approximately the region $x = 0$–26 cm. Although these are passive

Re (cm^{-1})	Organized motion (%)	No organization (%)	C_δ
2600 untripped	72	28	0.36
2600 tripped	60	40	0.35
7300 untripped	54	46	0.32
7300 tripped	33	67	0.25
14500 untripped	52	48	0.30
14000 tripped	34	66	0.25

TABLE 2. Statistics on the occurrence of coherent spanwise rollers, and growth rate for the $r = \frac{1}{4}$ layers

scalar images, with the dye carried in the low-speed side, the signals were linearly remapped in the upper half range of the obtained signals, by assigning a value of zero to the actual maximum signal obtained, thus making both free streams appear clear (dark). The pictures show the existence of coherent structures in the self-similar region (figure 3*a–c, f*). The large-scale structures for the $U_1 = 0.34$ m s^{-1} case were, in general, better defined and more frequently occurring than for the higher-speed cases. Nevertheless, organized motion was obtained for every case. Note that not all realizations displayed coherent structures in the self-similar region: examples are shown in figure 3(*d, e*). For all the cases presented, we examined all the available individual images in the $x = 14$–26 cm region, to extract statistics on the occurrence of large-scale organized structures. The accounting was performed in the spirit just mentioned: images like the ones in figure 3(*a–c*) were accounted as 'organized motion', whereas images like the ones in figure 3(*d, e*) as well as all those that appear ambiguous, were accounted as 'no organization'. All cases are quoted as Re (cm^{-1}) $\equiv (U_1 - U_2)/\nu$. The results appear in table 2. We notice that for untripped cases, the occurrence of coherent structures is more frequent for the lower Re (cm^{-1}) case than for two higher Re (cm^{-1}) cases (which yield similar statistics). When tripping occurs at higher Re (cm^{-1}), coherent structures become much less frequent. The two higher Re (cm^{-1}) cases, whether tripped or untripped, tend to yield similar statistics with each other.

3.2. *Shear layer growth rates*

The growth rate is an important measure of the layer, since it reflects all the parameters which influence the layer's development; the local thickness is therefore frequently used as a normalizing parameter. The panoramic views were averaged to extract information on the growth rate: selected results are shown in figure 4. The average images are shown in a binary colour table by threshold masking, to better display the edges of the layer. Examination of these averaged views reveals that the layer has two distinct regions of linear growth rate, depicted schematically in figure 5. Although the change in the spreading angle in the mixing layer is continuous (unlike the sketch in figure 5), the approximate region where the layer was seen to undergo a change in growth rate was at $Re = 8000$–14000 for untripped layers, which was a region related to the mixing transition; see the arrow marking the $Re = 12000$ location in figures 4(*a*) and 4(*c*). When the layer is tripped, the initial region is decreased in length (see arrow at $Re = 6000$ in figures 4(*b*) and 4(*d*)), suggesting that tripped layers tend to achieve far-field characteristics at an earlier downstream distance. This is consistent with the findings of Bell & Mehta (1990), who suggested that the growth rate of the untripped layer eventually decreases and tends towards that of a tripped layer at similar operating conditions. For the two higher Re cases, untripped layers have an initial region of no

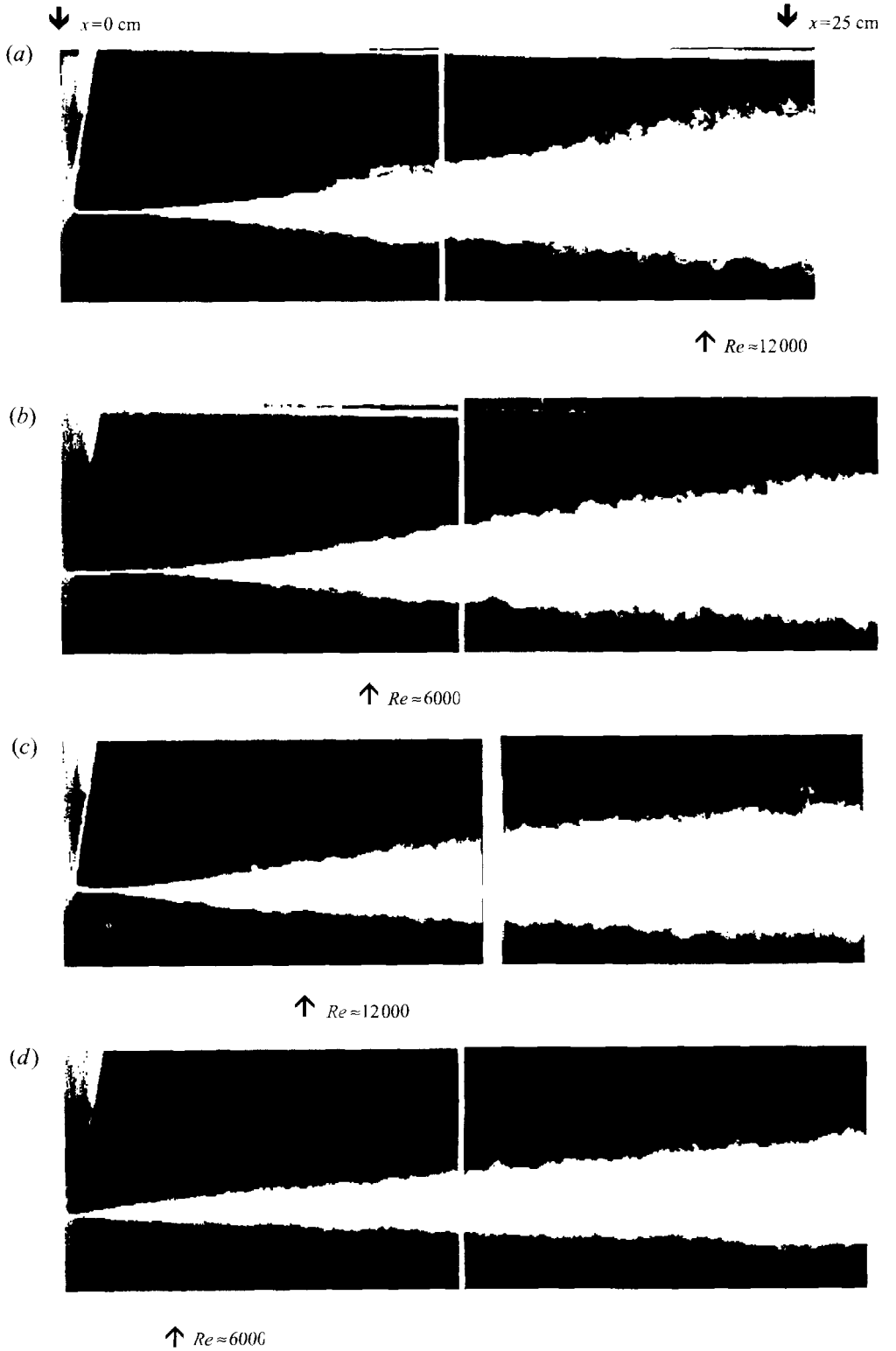

FIGURE 4. Averaged panoramic side view for $r = \frac{1}{3}$: (*a*) untripped $U_1 = 0.34$ m s^{-1}, (*b*) tripped $U_1 = 0.34$ m s^{-1}, (*c*) untripped $U_1 = 0.95$ m s^{-1}, (*d*) tripped $U_1 = 0.95$ m s^{-1}.

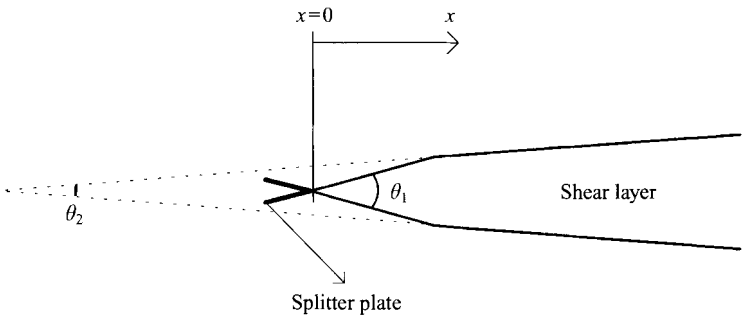

FIGURE 5. Schematic of the shear layer, showing two distinct linear-growth regions.

growth, and tripping causes the layer to start rolling up (growing) immediately after the splitter plate (compare figures 4(*c*) and 4(*d*)).

According to figure 5, two spreading rates are needed to characterize the growth pattern. The initial region, marked by a spreading angle θ_1, was measured to be about 15° for all cases. However, since this is a study of the fully developed region of the layer, the focus is to extract the growth rate for the further downstream region (marked by θ_2). To assign a measure of the growth rate in that region, where quantitative measurements were taken, the spreading rate was fitted to the Abramovich–Sabin formula:

$$\frac{\delta}{x} = C_\delta \frac{1-r}{1+r},$$

from which the 'constant' C_δ was obtained for each case (table 2). The values for C_δ show a considerable spread, which is most probably due to the effects of the initial conditions (initial boundary layers). The value of this coefficient is generally thought to depend on the initial and boundary conditions imposed by each facility, which may explain why other literature data show a wide range for $C_\delta \approx 0.25$–0.45 (Dimotakis 1991). The data show that for the two higher *Re* cases, tripping results in a diminished growth rate by 15% to 25%, consistent with the findings of other studies (Browand & Latigo 1979; Mungal *et al.* 1985; Bell & Mehta 1990). The growth rate for $U_1 = 0.34$ m s^{-1} is not affected by tripping, possibly because the layer has not reached far-field conditions within the imaged region. Also for the untripped cases, it is seen that as the velocity magnitudes are increased (*Re* is increased), the growth rate decreases.

3.3. *Plan views*

Figure 6 presents plan view images of the mixing layer for three untripped cases of $r = \frac{1}{4}$ and $U_1 = 0.34$, 0.95 and 1.90 m s^{-1}. These images are not processed except for background noise subtraction. Each image shows a field of view from $x = 20$–27 cm in a plane located at $y = -1$ cm, i.e. through the middle section of the layer. Flow is from left to right, with black representing pure high-speed fluid. The *Re* ranges from 11000 to 15000 for the lowest speed case, from 28000 to 38000 for the intermediate case and from 52000 to 69000 for the highest-speed case. In general, the spanwise organization of the layer, with superimposed streamwise vortices is evident and is similar to that shown by Bernal & Roshko (1986) for the lowest *Re* case, and similar to Clemens & Mungal (1992, 1995) at the highest *Re* cases. From the (few) available images, the estimated ratio of streamwise to spanwise vortex spacing was found to be in the range of 0.40–0.60. Occasionally, the spanwise structures also appear tilted, by $\pm 10°$ (see Browand & Troutt 1980).

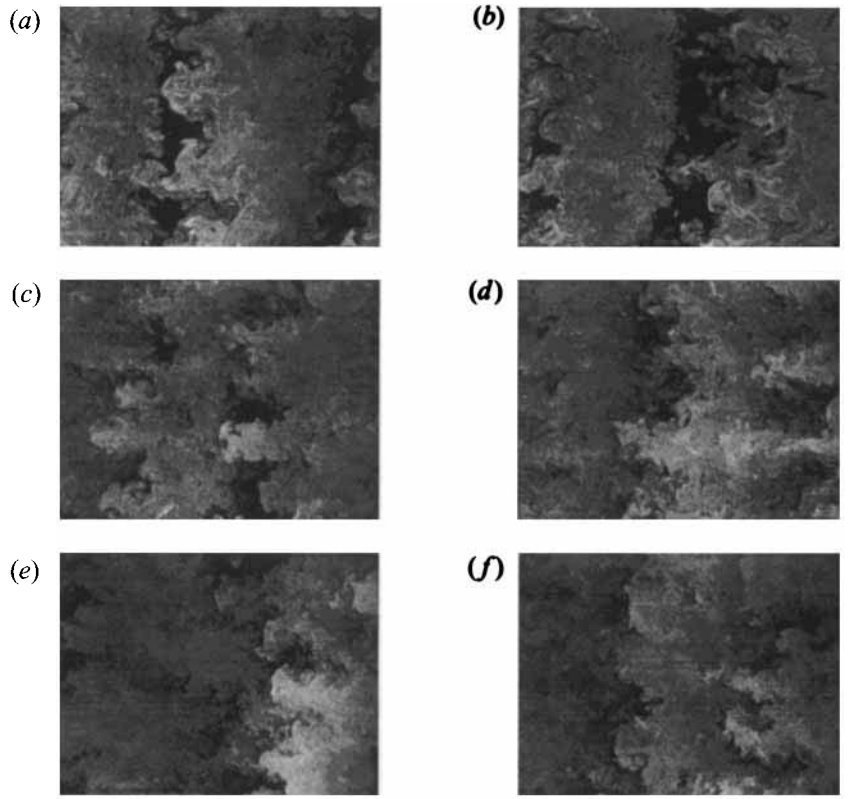

FIGURE 6. Plan views of untripped mixing layer, $r = \frac{1}{4}$. Views show $x = 20$–27 cm at $y = -1$ cm. Flow is left to right, high-speed fluid is black. (*a*, *b*) $U_1 = 0.34$ m s^{-1}, (*c*, *d*) $U_1 = 0.95$ m s^{-1}, (*e*, *f*) $U_1 = 1.90$ m s^{-1}.

4. Chemical reaction results

4.1. *Product profiles*

The chemical-reaction technique as described in §2.2.2 was implemented by placing reactants in the two free streams of the layer, and measuring the chemical product which is formed within the shear region. Three different cases were examined using chemical reactions: these were the three untripped $r = \frac{1}{4}$ layers with $U_1 = 0.34$ m s^{-1}, $U_1 = 0.95$ m s^{-1} and $U_1 = 1.90$ m s^{-1} corresponding to $Re = 14000$, 35000 and 64000, respectively, at the measuring station. The operating conditions for each case were identical to the passive scalar experiments to be described later, to allow comparisons between reacting and non-reacting results. For all cases, the camera's field of view was centred at $x = 25$ cm, with the actual imaged size being approximately 9.7×7.2 cm. Thus, the length resolved by each pixel on the imaging plane, had a nominal value of about 190 μm (again the resolution limitation was determined by the laser sheet thickness). For each case, a set of 'flip' experiments was conducted at $\phi = 16$ and at $\phi = \frac{1}{16}$; as mentioned before, these values are believed to adequately represent the two limits $\phi \to \infty$ and $\phi \to 0$. The $\phi = 16$ cases were run with the acid/dye solution in the high-speed side, and the base solution in the low-speed side; for the $\phi = \frac{1}{16}$ cases the chemical solutions were exchanged in the two free streams. The imaged fluorescence represents the instantaneous product concentration, $C_P(y, \phi)$, at a given location (y) and a given stoichiometry (ϕ).

An important conclusion that will be shown later, when the passive scalar results are

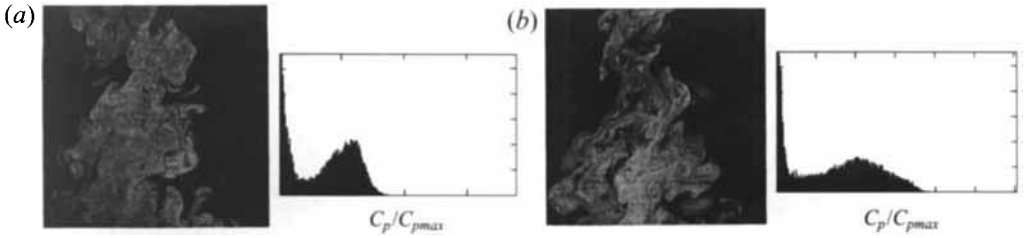

FIGURE 7. Chemical-reaction side views for the $Rx/\lambda = 18$ layer ($U_1 = 0.34$ m s^{-1}, $Re = 14000$). (*a*) $\phi = \frac{1}{16}$, (*b*) $\phi = 16$.

presented, is that the parameter that uniquely defines the character of the mixing field is the 'pairing parameter', Rx/λ, where $R = (1-r)/(1+r)$, $r = U_2/U_1$, x is the downstream distance, and λ is the initial instability wavelength. To aid in this discussion, the three cases to be presented here will be labelled by their pairing parameters of 18, 30 and 42 in subsequent figures.

The mixing layer width, δ, was defined by the two points across the layer at which the average product (dye) concentration $\overline{C_P}(y)$ had dropped to 1 % of its peak value. The widths obtained are in very good agreement with the measured widths from the passive scalar experiment for each layer. Thus, the pairing parameter and the Reynolds number for each case have the same values quoted in the passive scalar method as listed in table 1.

Some definitions are now necessary to follow the data analysis. The maximum possible signal that can be achieved, $C_{P\,max}$, is a function of the seeding density of the fluorescein dye in the free stream (C_{10} when the dye is placed in the high-speed stream, C_{20} when the dye is placed in the low-speed stream), and of the fluorescence 'turn on' mixture fraction. It can easily be shown that $C_{P\,max} = C_{10}\phi/(1+\phi)$ (dye seeded the high-speed side), or $C_{P\,max} = C_{20}\,1/(1+\phi)$ (dye seeded in the low-speed side). For each run, $C_{P\,max}$ was monitored through a reference static cell. By averaging all images for each case, the average chemical-product concentration across the layer is defined as:

$$\theta_1(y) = \frac{\overline{C_P}(y, \phi \to \infty),}{C_{10}},$$

$$\theta_2(y) = \frac{\overline{C_P}(y, \phi \to 0),}{C_{20}}.$$

The product thickness, δ_P, is defined as the total amount of product integrated across the entire layer. The normalized product thickness(es) is defined as

$$\frac{\delta_{P_1}}{\delta} = \int_{-0.5}^{+0.5} \frac{\overline{C_P}(y, \infty)}{C_{10}} \mathrm{d}(y/\delta),$$

and

$$\frac{\delta_{P_2}}{\delta} = \int_{-0.5}^{+0.5} \frac{\overline{C_P}(y, 0)}{C_{20}} \mathrm{d}(y/\delta),$$

Figures 7, 8 and 9 show typical (processed) images for the three layers examined. Each layer was run at $\phi = \frac{1}{16}$ and $\phi = 16$, with samples shown, respectively, in (*a*) and (*b*). The organization in the flow is apparent, as is the variability within a given case. The layer, containing product, shows a range of grey scales, while the free streams, being product free, appear black. To the right of each image is a histogram of the

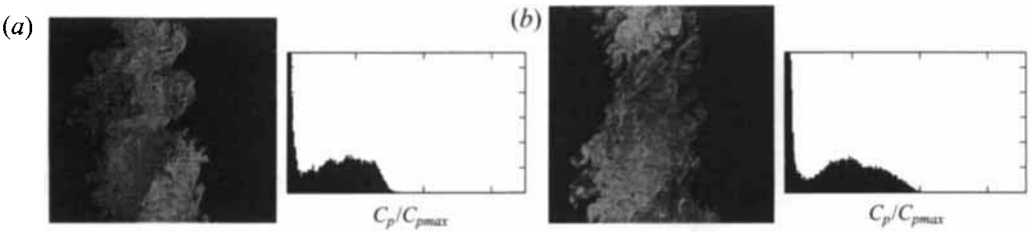

FIGURE 8. Chemical-reaction side views for the $Rx/\lambda = 30$ layer ($U_1 = 0.95$ m s^{-1}, $Re = 35000$). (*a*) $\phi = \frac{1}{16}$, (*b*) $\phi = 16$.

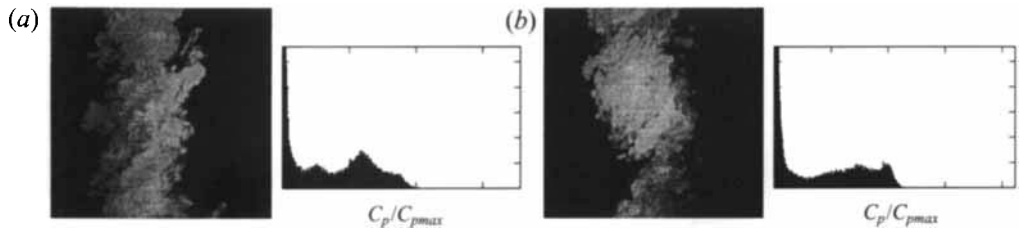

FIGURE 9. Chemical-reaction side views for the $Rx/\lambda = 42$ layer ($U_1 = 1.90$ m s^{-1}, $Re = 64000$). (*a*) $\phi = \frac{1}{16}$, (*b*) $\phi = 16$.

obtained values of C_P normalized by the maximum reference signal ($C_{P\,max}$). It is interesting to see that the maximum signal is never attained (considering the resolution requirements), and that the signals for $\phi = 16$ are higher than for $\phi = \frac{1}{16}$.

The following results were calculated based on about 100 images acquired for each case. Figure 10 shows the average chemical-product profiles across the layer for the two stoichiometric ratios, for each case-layer. By integrating the product concentration profile across the layer's width (which is essentially the area under each average product profile), the total amount of chemical product formed (for each stoichiometric ratio) was obtained. The results are summarized in table 3 (other entries are explained later), where the total product is given in the form of a normalized product thickness. It is interesting to notice that by normalizing δ_P by the layer's width δ, the product thickness essentially represents the volume fraction of chemical product in the layer.

Some observations are now in order. First, for all cases, more product is formed for $\phi = 16$ than for $\phi = \frac{1}{16}$; the plots in figure 10 show that the $\phi = 16$ profile is always higher than the $\phi = \frac{1}{16}$ profile; this observation is consistent with higher entrainment of fluid from the high-speed side of the layer (Mungal & Dimotakis 1984; KD). Furthermore, for the least developed case ($U_1 = 0.34$ m s^{-1}, $Rx/\lambda = 18$) both (flip) profiles are symmetric (with respect to $y = 0$), whereas for the two more developed layers the curves are tilted towards the side of the mixing layer that carries the lean reactant (the base solution). The plots in figure 10 reveal that the layer evolves from $Rx/\lambda = 18$ to $Rx/\lambda = 30$. Symmetric product profiles, almost identical to these in figure 10(*a*), were obtained by KD for their $Rx/\lambda \approx 16$ layer, which is now believed to be not fully developed.

Table 3 shows a slight increase in the volume fraction of chemical product as the layer becomes more developed; however, the quoted values are within the noise and data processing uncertainties. One of the goals of the present experiments was to measure the amount of chemical product within a liquid layer as *Re* increases and the layer reaches its fully developed state. The product thicknesses from table 3, are plotted in figure 11 for the high-ϕ and the low-ϕ. On the same plots are marked the liquid-phase results of KD (only layers past the mixing transition are considered) and all the

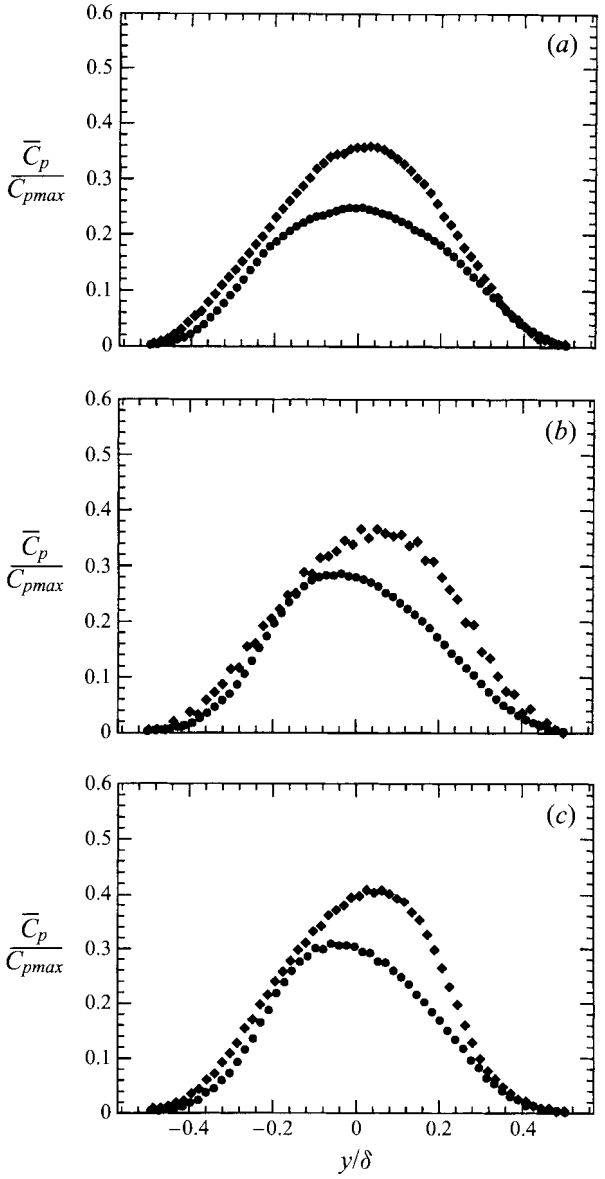

FIGURE 10. Average chemical-product profiles at $\phi = 16$ (◆) and $\phi = \frac{1}{16}$ (●). (*a*) $Rx/\lambda = 18$, (*b*) $Rx/\lambda = 30$, (*c*) $Rx/\lambda = 42$.

	$\frac{\delta_{P_1}(\phi = 16)}{\delta}$	$\frac{\delta_{P_2}(\phi = \frac{1}{16})}{\delta}$	C_M	P_M	E
$Rx/\lambda = 18$ ($Re = 14000$)	0.171	0.125	0.578	0.296	1.37
$Rx/\lambda = 30$ ($Re = 35000$)	0.174	0.128	0.576	0.302	1.36
$Rx/\lambda = 42$ ($Re = 64000$)	0.179	0.132	0.576	0.311	1.36

TABLE 3. Chemical product, and estimated mixed-fluid quantities based on chemical reaction data

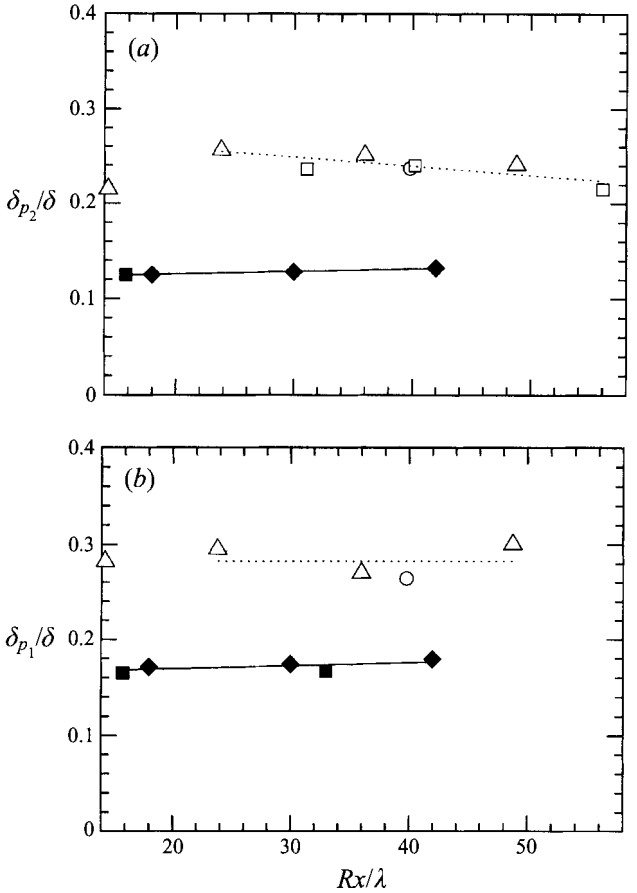

FIGURE 11. Normalized product thickness *vs.* pairing parameter for the straight turbulent shear layer. (*a*) low-ϕ layers, (*b*) high-ϕ layers. ◆, present study (liquid); ■, KD (liquid); ○, Mungal & Dimotakis (gas); □, Mungal *et al.* (gas); △, Frieler (gas).

available gaseous-phase results. The present results show that the product volume-fraction in liquid layers increases slightly when the layer becomes more developed. The low-ϕ case (figure 11*a*) shows a 5.5% increase in product within the examined range. The high-ϕ data (figure 11*b*) also favours an increase of 4.7% in going from $Rx/\lambda = 18$ to $Rx/\lambda = 42$. The present results are consistent with KD: the two KD points show a 1.2% increase from $Rx/\lambda = 16$ to $Rx/\lambda = 33$, whereas an increase of 1.7% is seen in going from $Rx/\lambda = 18$ to $Rx/\lambda = 30$ (present work).

The change in the shape of the product-concentration profiles as the layer becomes more fully developed, marks an evolution in the mixing field of the layer. It is important to quantify this evolution in terms of (i) the distribution and the amount of mixed fluid in the layer, and (ii) the average composition of mixed fluid. The following section will provide insight on these issues.

4.2. *Mixed fluid properties*

The importance of performing a pair of flip experiments for each layer, lies in the ability to estimate mixed-fluid properties based on chemical-product data in the limit of 'very large' and 'very small' ϕ. These estimates are considered to be resolution-free, since the chemical-reaction technique provides average product concentrations which are not affected by the spatial resolution requirements.

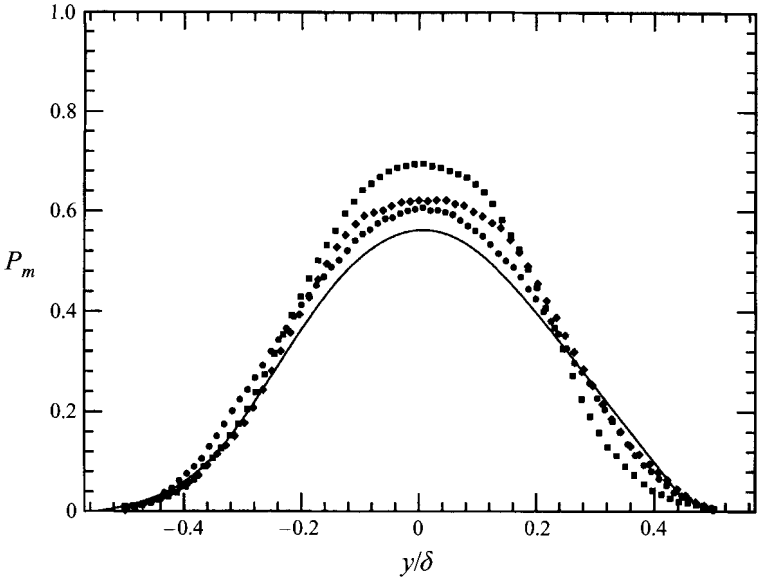

FIGURE 12. Mixed-fluid probability profiles for liquid layers, based on chemical-reaction data. ●, Rx/λ = 18; ◆, 30; ■, 42; ——, 16 (KD).

Following the analysis outlined by Koochesfahani (1984), several mixed-fluid properties were calculated. The probability of finding mixed fluid (at any composition) across the layer,

$$P_m(y) = \int_{\epsilon}^{1-\epsilon} P(\xi, y)\,\mathrm{d}\xi$$

(ϵ denotes a small positive number to exclude pure high-speed and pure low-speed fluid from being accounted), was estimated through: $P_m(y) = \theta_1(y) + \theta_2(y)$, and is shown in figure 12 for the three layers. The total probability of mixed-fluid, P_M, which is the area under each $P_m(y)$ profile, is given in table 3, and represents the volume fraction of the layer occupied by molecularly-mixed fluid. The data suggests only a very slight mixing enhancement as the layer becomes more developed.

The average concentration of mixed fluid, $C_m(y)$, was approximated through the relation $C_m(y) = \theta_1(y)/(\theta_1(y) + \theta_2(y))$, and is shown in figure 13. The profile obtained by KD is also plotted, as well as the profile pertaining to the gaseous layer of Mungal & Dimotakis (Koochesfahani (1984) compiled the Mungal curve). It is interesting to focus first on the shape of these profiles in the central 50% of the layer ($-0.25 \leqslant y/\delta \leqslant 0.25$). The least developed layer ($Rx/\lambda = 18$) and the KD layer ($Rx/\lambda = 16$) are relatively flat (consistent with a non-marching p.d.f., figure 1*a*). The two more developed layers (present study) have a mild slope: the mixed-fluid concentration is seen to develop a bias towards the side of the layer to which it is closer. The modest slope in the $C_m(y)$ curve suggests that the p.d.f. would have a slight variation across the layer. However, the slope for the present liquid layers is not nearly as large as that of the gaseous result of Mungal. It is obvious that Schmidt-number effects persist in the layer even at these high values of the pairing parameter, where the layer is fully developed; further comparisons between liquid and gaseous layers are discussed later. Next, the regions of the layer which are close to the free stream are considered. As the edges of the low-speed side are approached, the three layers of the present study have a very similar shape, which differs from the flat response of the KD profile. Towards

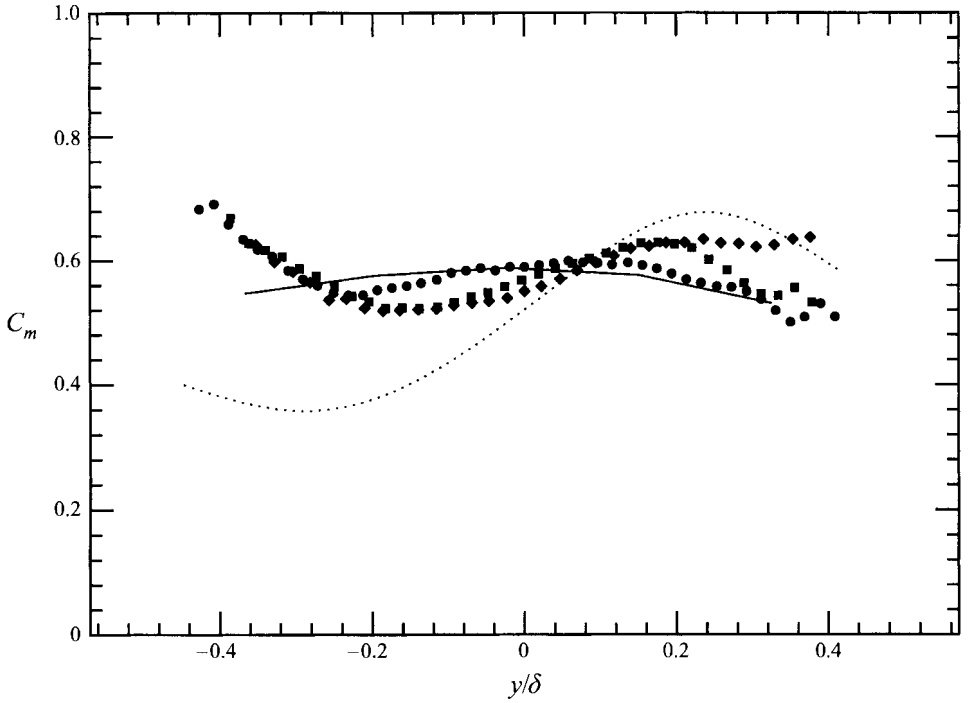

FIGURE 13. Average mixed-fluid composition, based on chemical-reaction data. ●, $Rx/\lambda = 18$ (liquid); ◆, 30 (liquid); ■, 42 (liquid); ——, 16 (liquid) KD; · · · ·, 40 (gas) Mungal.

the high-speed edge, each layer has a different shape. The low probability of finding mixed fluid near the edges of the layer (figure 12) results in poor signal-to-noise ratio in those regions, and hence the results in figure 13 are more reliable towards the middle section of the layer.

Finally, the total average mixed-fluid concentration integrated across the layer, C_M, was estimated through $C_M = \delta_{P_1}/\delta_{P_1} + \delta_{P_2}$. The results appear in table 3; KD estimated a value of $C_M = 0.57$. If it is assumed that the reactants mix (on average) at the ratio at which the free-stream fluids are entrained, then the values for C_M can be used to make an estimate of the entrainment ratio E, based on:

$$C_M = \frac{E}{1+E}.$$

The results are shown in table 3, which shows E to be about the same (1.36–1.37) for all three layers. The formula proposed to Dimotakis (1986) predicts a value of ≈ 1.41 for the present study's operating conditions. Possible reasons for this discrepancy are: (i) the actual large-scale-structure spacing-to-position ratio varies from that proposed by Dimotakis' theory, and (ii) the composition ratio of mixed-fluid is not necessarily the same as the entrainment ratio of the two free-stream fluids.

5. Passive scalar results

5.1. *Quantitative images*

The passive scalar technique, as described in §2.2.1., was applied to nine different cases. The acquired images for each case, after being corrected, represent the data used to extract the quantitative results. In this work, we define the mixture fraction, ξ, to be

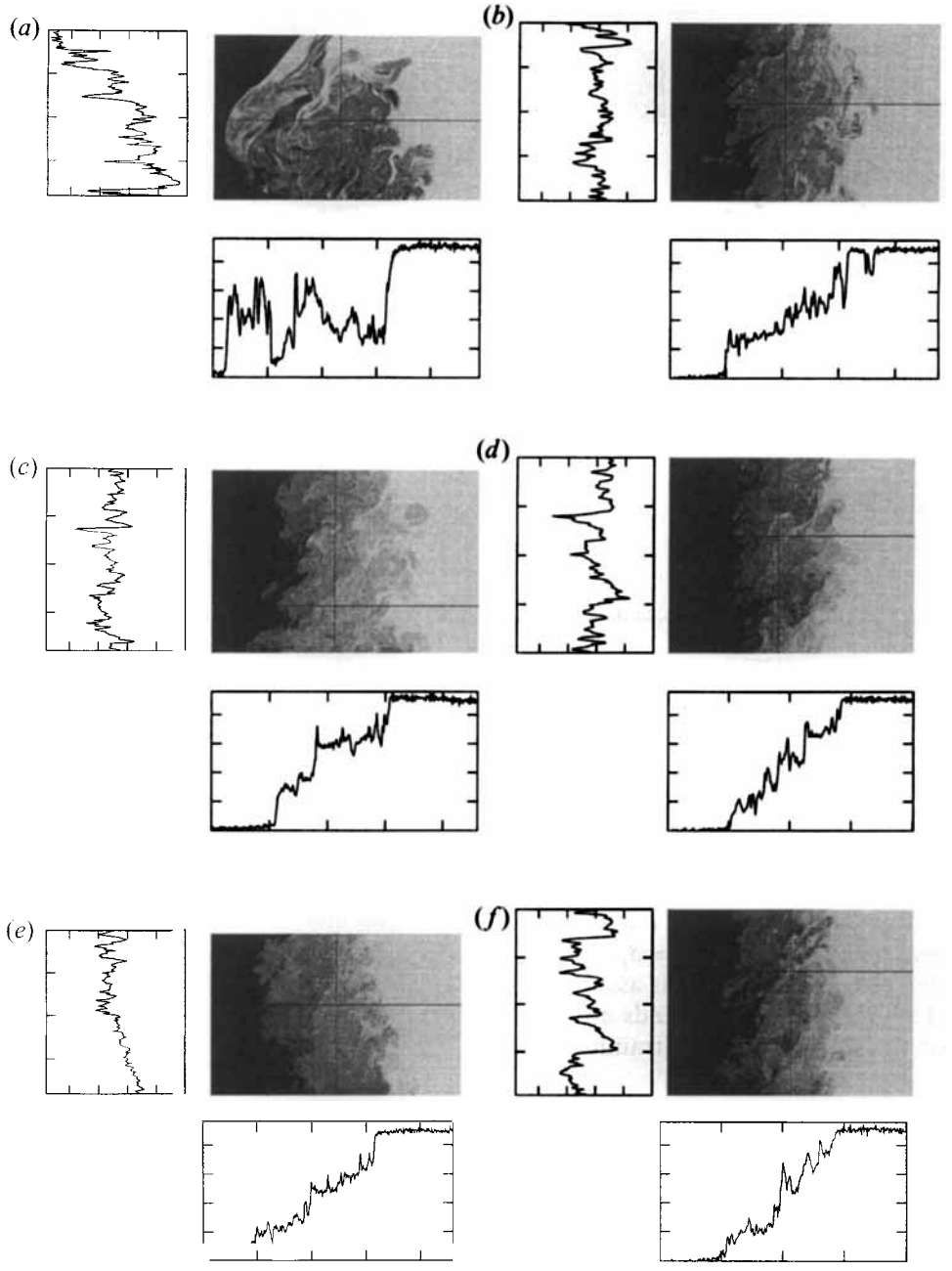

FIGURE 14(*a–f*). For caption see facing page.

the fraction of high-speed stream fluid in the mixture. By averaging all the images for each case, the thickness δ of the layer at the $x = 25$ cm location downstream of the splitter plate is obtained with δ defined as the width where the average concentration had changed by 1% from the free-stream value; these widths were in very good agreement with the three corresponding chemically reacting cases. The resulting δ and the corresponding Re for all cases appear in table 1.

Figure 14 shows samples of corrected images for all cases examined. The flow

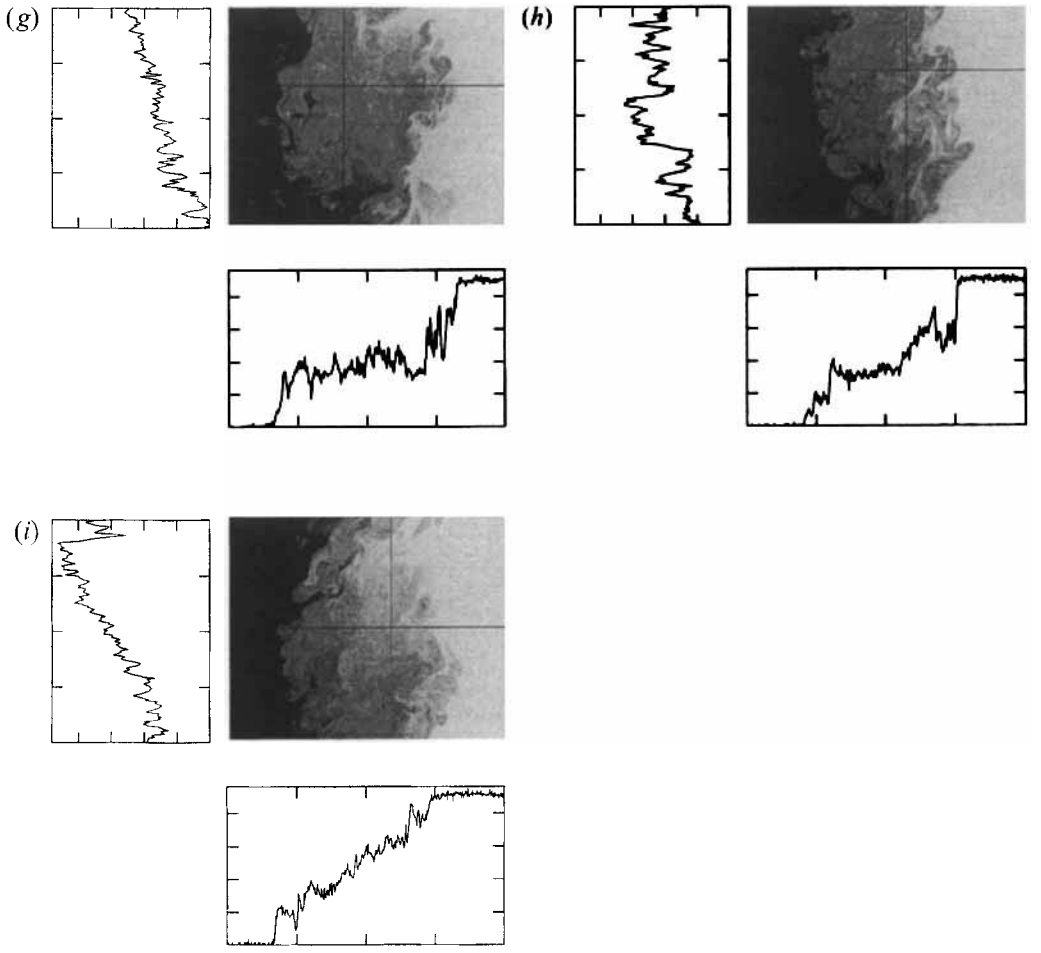

FIGURE 14. Side view passive scalar images for: (*a*) untripped $r = \frac{1}{4}$ $U_1 = 0.34$ m s^{-1}, (*b*) tripped $r = \frac{1}{4}$ $U_1 = 0.34$ m s^{-1}, (*c*) untripped $r = \frac{1}{4}$ $U_1 = 0.95$ m s^{-1}, (*d*) tripped $r = \frac{1}{4}$ $U_1 = 0.95$ m s^{-1}, (*e*) untripped $r = \frac{1}{4}$ $U_1 = 1.90$ m s^{-1}, (*f*) tripped $r = \frac{1}{4}$ $U_1 = 1.90$ m s^{-1}, (*g*) untripped $r = \frac{1}{2.6}$ $U_1 = 0.70$ m s^{-1}, (*h*) tripped $r = \frac{1}{2.6}$ $U_1 = 0.70$ m s^{-1}, (*i*) untripped $r = \frac{1}{2.6}$ $U_1 = 1.05$ m s^{-1}. For each image, intensity distribution plots are shown along a streamwise cut (left), and a cross-stream cut (bottom).

direction is from top to bottom, with the low-speed side (uniform bright area) being at the right side in each image. Perpendicular cuts in the streamwise and the cross-stream direction are shown to the right and bottom of each image and represent concentration distributions across the layer. The various cases are represented as follows: figures 14(*a*)–14(*f*) examine 6 cases for $r = \frac{1}{4}$, $U_1 = 0.34$, 0.95 and 1.90 m s^{-1} both untripped and tripped. Figures 14(*g*)–14(*i*) examine 3 cases for $r = \frac{1}{2.6}$ and $U_1 = 0.70$ and 1.05 m s^{-1}. It is illustrative to follow each case in detail.

For the $Re = 14000$ ($r = \frac{1}{4}$, $U_1 = 0.34$ m s^{-1}) case, shown in figure 14(*a*), well-defined coherent structures appear, consistent with the observations from the panoramic views. The dye concentration (and hence the mixture fraction) across the layer tends to be uniform, as in the KD study. However, ramps (gradients) in the concentration field across the layer were also observed, both in the streamwise direction (see plot to the left of image), and in the cross-stream direction (no example is shown). It is interesting to mention that structures were found to be uniform in a streamwise cut and ramped

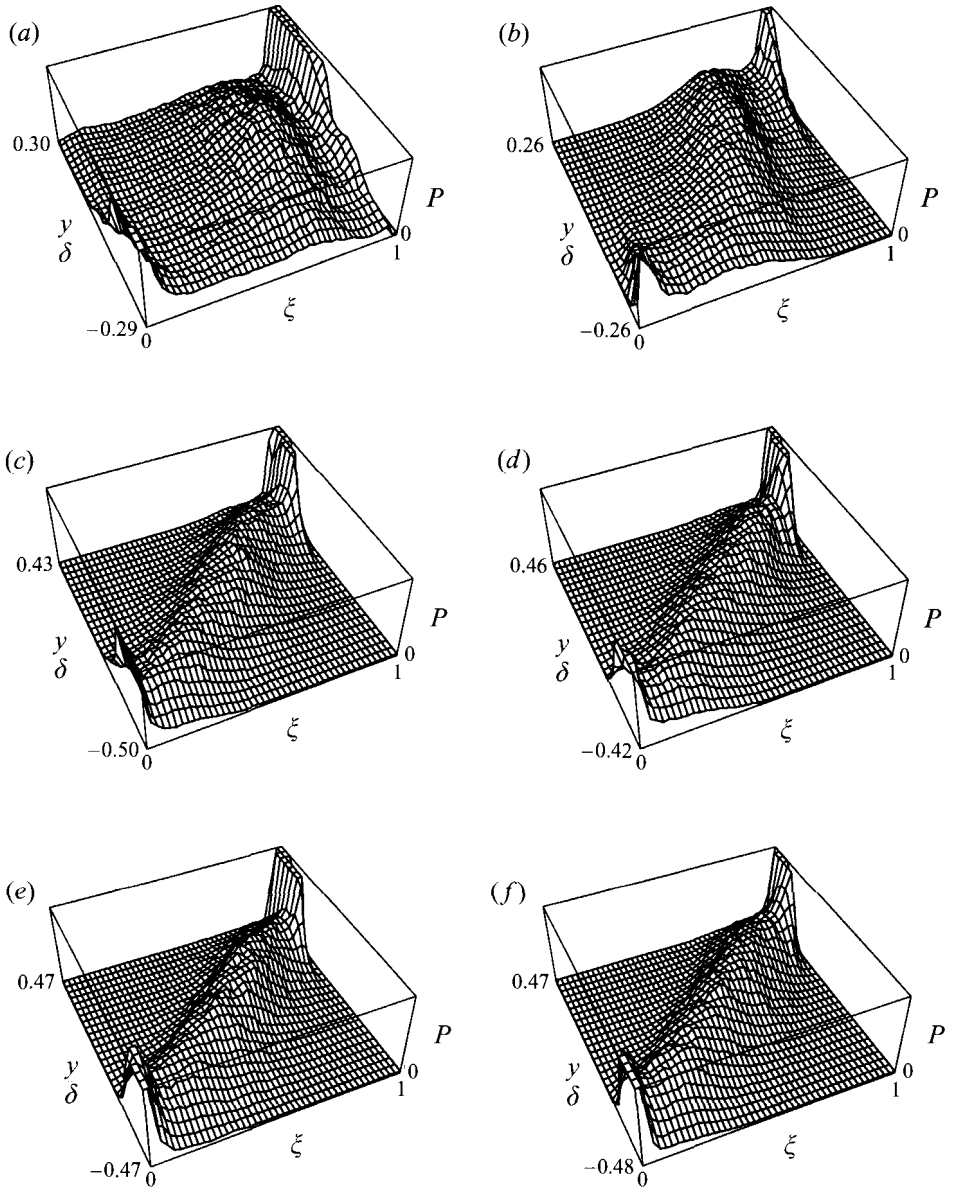

FIGURE 15(*a–f*). For caption see facing page.

in a cross-stream cut, and vice versa. Furthermore, a broad range of mixture fraction values exists within each structure. The tripped counterpart of this low-*Re* case shows similar characteristics (figure 14*b*), and is also characterized by a wide range of mixture fraction values.

At the higher speed cases $Re = 35000, 64000$ ($r = \frac{1}{4}$, $U_1 = 0.95, 1.90$ m s^{-1}), the layer appears to have developed much finer scales (figure 14*c*). Here, the cuts frequently show the existence of strong concentration ramps, both in the cross-stream direction, and in the streamwise direction (figure 14*e*). Again, not all realizations display ramps, and uniformity of the mixed-fluid composition can occur, but at a much lower frequency. In general though, the departure from structures dominated by a preferred mixture fraction value is significant for the two higher *Re* cases. The tripped layers at

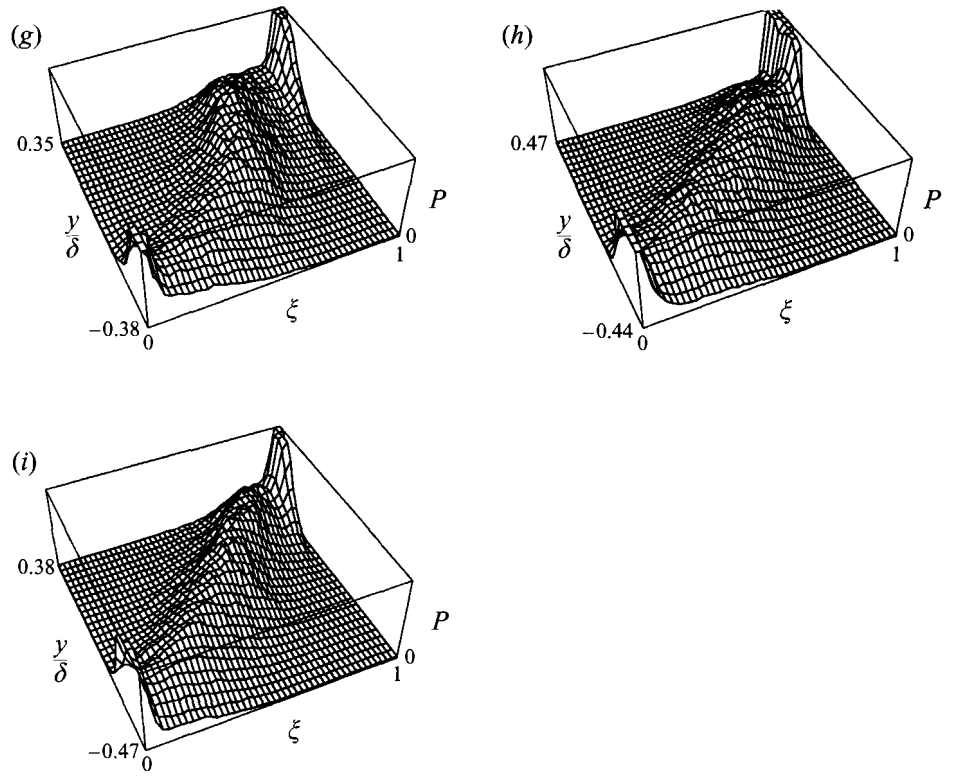

FIGURE 15. Mixture fraction p.d.f.s for: (*a*) untripped $r = \frac{1}{4}$ $Re = 14000$, (*b*) tripped $r = \frac{1}{4}$ $Re = 13500$, (*c*) untripped $r = \frac{1}{4}$ $Re = 35000$, (*d*) tripped $r = \frac{1}{4}$ $Re = 27000$, (*e*) untripped $r = \frac{1}{4}$ $Re = 64000$, (*f*) tripped $r = \frac{1}{4}$ $Re = 54000$, (*g*) untripped $r = 1/2.6$ $Re = 18500$, (*h*) tripped $r = 1/2.6$ $Re = 14000$, (*i*) untripped $r = 1/2.6$ $Re = 27000$. Probability axis clipped at approximately 4.5.

the same operating conditions (figures 14*d* and 14*f*), show a behaviour similar to their untripped counterparts.

For the second set of experiments at the speed ratio of $r = \frac{1}{2.65}$, the following are observed. The $Re = 18500$ ($U_1 = 0.70$ m s^{-1}) case in figure 14(*g*), shows concentration profiles across the layer which tend to be uniform, but again gradients are not uncommon. The images show evidence of a well-defined K–H roller for 74% of the cases. When tripping the boundary layer for this case (figure 14*h*), the layer developed concentration gradients more frequently. Notice that concentration gradients may not be smooth from one side to the other across the layer, and can occur in 'steps' of visible scale. Finally, figure 14(*i*) shows images of the $Re = 27000$ ($U_1 = 1$ m s^{-1}, $r = \frac{1}{2.65}$) case. As before, higher-velocity magnitudes lead to the development of concentration gradients within the layer. Still, few images displayed uniformity, with different preferred mixture fraction levels for different images. About 50% of the images showed evidence of K–H rollers.

We feel that examination of the individual images in terms of appearance and composition distribution is useful, since it allows a better interpretation of the p.d.f. by revealing how the statistics evolve from single images to the whole data volume.

5.2. *Passive scalar p.d.f. and average concentrations*

The probability density function (p.d.f.) of the mixture fraction ξ at a given location y across the layer is given by

$$\text{p.d.f.}(\xi, y)\,\mathrm{d}\xi = \text{Probability}\{\xi \leqslant \xi(y) \leqslant \xi + \Delta\xi\},$$

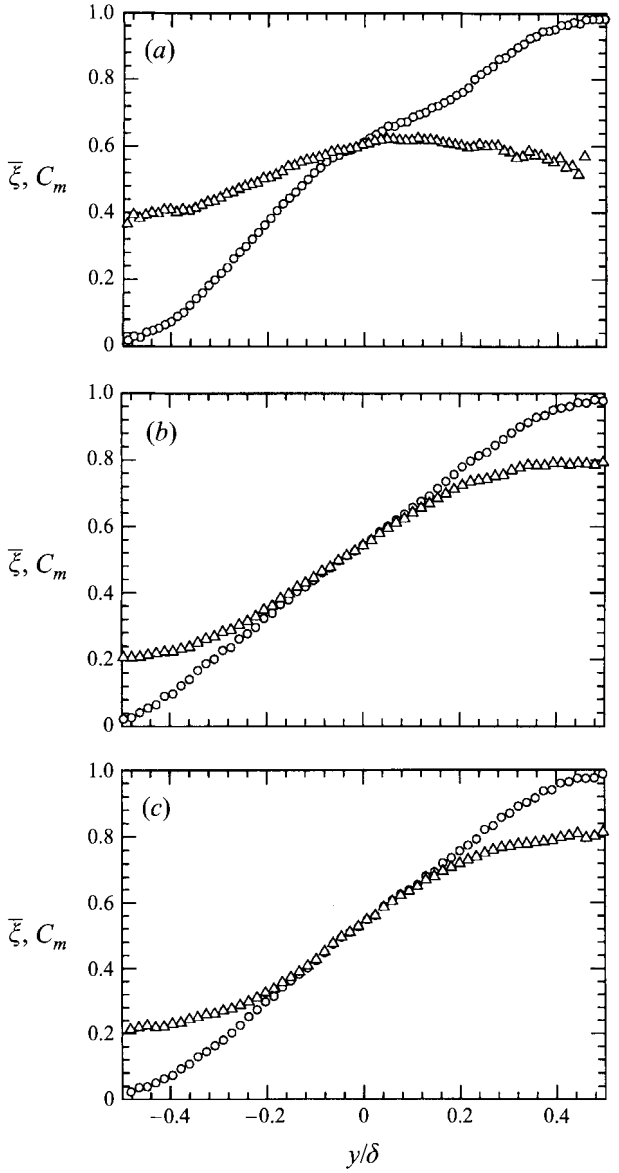

FIGURE 16. Average composition, and mixed-fluid average composition for untripped layers: (*a*) $Re = 14000$ ($U_1 = 0.34$ m s^{-1}, $Rx/\lambda = 18$), (*b*) $Re = 35000$ ($U_1 = 0.95$ m s^{-1}, $Rx/\lambda = 30$), (*c*) $Re = 64000$ ($U_1 = 1.90$ m s^{-1}, $Rx/\lambda = 42$). ○, $\bar{\xi}$; △, C_m.

where all the pixels in a given volume of an image are treated as corresponding to one y location across the layer (they are counted, not averaged).

The p.d.f.s for all the cases are shown in figure 15 (where P denotes the above-defined probability). The average fluid concentration (mean), $\bar{\xi}(y)$, and the average mixed-fluid concentrations (mixed mean), $C_m(y)$, across the layer are shown in figure 16 for the three $r = \frac{1}{4}$ untripped layers corresponding to the three chemically reacting layers presented earlier. In defining the mixed mean, mixture fraction values to within 10% of the free stream's value were considered to be unmixed fluid.

Figure 15(*a*) shows that for the $Re = 14000$ ($r = \frac{1}{4}$) case, the p.d.f. is non-marching, with the most probable mixture fraction values at $\xi \approx 0.68$. A broad range of mixture

fraction values exists at each y-location. This is attributed to the streamwise concentration gradients, and to the structure-to-structure variations that were previously seen to exist in different realizations. There is penetration of unmixed fluid into the layer, similar to that reported by KD. In the tripped case under the same operating conditions (figure 15*b*), the non-marching behaviour is preserved, but with some modifications. The average and the mixed-fluid average profiles for the $Re = 14000$ untripped case are shown in figure 16(*a*). Notice how the two curves have a different shape across the layer.

For the two higher Re cases $Re = 35000$ and $Re = 64000$, at the same $\frac{1}{4}$ speed ratio, the shape of the p.d.f. becomes marching (figure 15*c*, *e*). The two cases display very similar characteristics. The scalar field now tends to locally favour the free stream to which it is closer. Pure unmixed fluid deep within the layer is much less frequent than in the lowest Re case. The marching p.d.f.s are the reflection of individual images exhibiting concentration gradients in the cross-stream direction across the layer. The present marching p.d.f.s are in sharp contrast to the measurements of KD ($Re = 23000$, also liquid phase) and of Konrad ($Re \approx 32000$, gas phase), although the Reynolds numbers are comparable. Tripping in both these two higher Re cases does not alter the marching character of the p.d.f. (figure 15*d*, *f*). The average and the mixed-fluid average distribution curves are shown in figures 16(*b*) and 16(*c*) for (untripped) $Re = 35000$ and $Re = 64000$, respectively. The difference between mean and mixed mean profiles is now less pronounced.

Finally, the layers at the speed ratio of $r = \frac{1}{2.65}$ are examined. At $Re = 18500$ ($U_1 = 0.7$ m s^{-1}) the p.d.f. (figure 15*g*) shows a character that is non-marching for a large extent of the layer, with a marching break-out towards and close to the low-speed side. A similar 'dual behaviour' p.d.f. was measured in an axisymmetric gaseous shear layer by Clemens & Paul (1995). This seems to be the shape of a p.d.f. that is prior, but about to 'transition' from non-marching to marching behaviour. Upon tripping under the same operating conditions, the p.d.f. becomes marching (figure 15*h*). For the (untripped) $Re = 27000$ case, the p.d.f. is marching (figure 15*i*). Again it appears that, for a given speed ratio, the p.d.f. evolves to marching as the Re is increased. It is also remarkable that for the $Re = 18500$ case, tripping makes the layer achieve a state similar to that which is achieved by an increase in Re.

5.3. *The resolution issue*

The issue of resolution comes up as a result of the inability of the measuring technique (laser-camera system) to resolve the smallest spatial or temporal scales (diffusion scales) which control the mixing process.

The shortest turbulence timescale relevant to mixing was estimated (for the highest Re case) to be on the order of 1 μs. This number corresponds to the convection time of the local molecular diffusion scale. On the other hand, the sum of the duration of a laser pulse (for both lasers used) and of the fluorescence lifetime is less than 20 ns. It is then clear that all images are temporally resolved.

For all acquired passive-scalar images, the actual size of the imaged region is approximately 7.2×5.4 cm in the y- and x-direction, respectively. The experimentally resolved lengthscale, which is the area imaged on each pixel, is therefore about 140 μm in each direction on the imaging plane (these are nominal values, as the Nyquist sampling theorem must also be considered). However, it is the z-direction which represents the worse dimension, L, in the achieved spatial resolution, with the thickness of the laser sheet being about 750 μm (for the CVL).

The smallest pertinent physical lengthscale is the mass diffusion scale, λ_B (equation

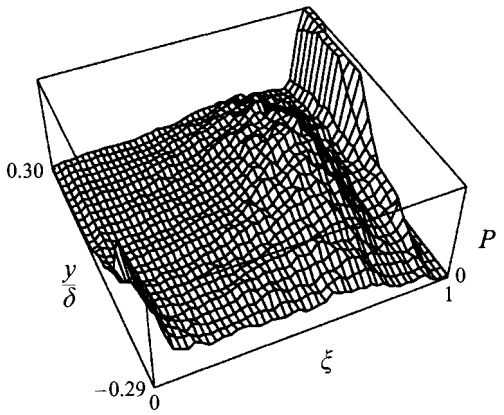

FIGURE 17. Mixture fraction p.d.f. for the $Re = 14000$ ($r = \frac{1}{4}$) layer, where the resolution was worsened to $L/\lambda_B \approx 1600$ through data (pixel) binning.

(1)). The estimated λ_B ($Sc \approx 2000$ for water/fluorescein, see Ware *et al.* (1983)), and the relative resolution, L/λ_B, are given in table 1 for all untripped cases. (Since the interest lies in examining the effects of resolution deterioration as a result of an increase in Re, only untripped cases need be considered for comparison purposes.) The severe resolution discrepancy for all cases strongly suggests that the presented passive scalar p.d.f.s (and all estimates based upon them) are incorrect. However, even then, it is noteworthy that a sweeping change – from non-marching to marching – occurs in the p.d.f. when going from $Re = 14000$ (with $L/\lambda_B \approx 800/1$) to $Re = 35000$ (with $L/\lambda_B \approx 1750/1$). Two possible reasons can be invoked to explain this: (i) the scalar field has been shown from the previous chemical reaction results to undergo a change as the Reynolds numbers increases, but the change was seen to be modest and does not argue for such a large change in the p.d.f., and (ii) resolution deterioration, beyond a certain value of the ratio L/λ_B, causes a p.d.f. to become 'marching'. We now wish to consider the issue of whether resolution can cause the observed change in the p.d.f.-shape.

First, notice that a non-marching p.d.f was obtained in the present study with $L/\lambda_B \approx 800/1$, while KD also obtained a non-marching p.d.f. with a 50% worse resolution of $L/\lambda_B \approx 1200/1$. This provides a clue that resolution deterioration is not the only cause for the observed change in the shape of the p.d.f. Now, for the $Re = 35000$ layer, with $L/\lambda_B \approx 1750/1$, we measured a marching p.d.f. Assuming that the flow structure remains the same (all cases deal with a non-reacting, water mixing layer), the question focuses on whether a (small) deterioration of the relative resolution from 1200 to 1750 is introducing a bias that would sharply alter the shape of the p.d.f.

A direct test was thus performed to check the effect of relative resolution to the character of the measured p.d.f.s. The resolution of the $Re = 14000$ case was worsened and made similar to that of the $Re = 35000$ case. This was done via pixel binning: the data of the $Re = 14000$ cases was averaged in an area over 12 pixels in the y-direction ($L_y \approx 1650$ μm), and over 8 pixels in the x-direction ($L_x \approx 1100$). Thus, the 'worse' dimension is now found on the imaging (x, y)-plane, and since $\lambda_B \approx 1$ μm (table 1), a value of $L/\lambda_B \approx 1700/1$ is obtained. The p.d.f. result for this pixel-binned case appears in figure 17. The non-marching character is preserved (compare to figure 15*a*). Hence, for the present layers the change in the shape of the p.d.f. as Re increases cannot be attributed solely to the deterioration of the measurements' resolution, or the above test would have yielded a marching p.d.f. Our inability to change the p.d.f. implies that a

change has occurred in the flow at sub-pixel dimensions, to which the passive scalar approach is known to be sensitive.

Finally, we wish to mention that all present case-layers have also been measured using the Nd:YAG system (Karasso & Mungal 1992), where the laser sheet thickness was about 400 μm. For each case, the obtained p.d.f. was exactly identical to the present results with the CVL, while the corresponding L/λ_β was about twice as good. Concluding, it appears that amelioration or worsening of the resolution by a factor of ≈ 2 is not critical given the $O(10^3)$ overall removal from the Batchelor scale, for all cases in discussion.

6. Discussion of results

6.1. *Comparisons of chemically reacting and passive scalar results*

We are now in a position to critically examine the effects of resolution on the passive scalar results presented earlier. First, the calculated product based on the p.d.f. (we assume a fast and irreversible reaction at a certain ϕ) is compared to the chemical-reaction measurements. The comparisons, for the three untripped cases at $r = \frac{1}{4}$ (and for both stoichiometries) are shown in figure 18. All plots show the expected overestimation of the amount of mixed (and hence reacted) fluid by the passive scalar technique. For the $Rx/\lambda_B = 18$ layer (figure 18*a*) it is seen that although the calculations (for both ϕ) are in error with respect to the measured product profiles, still the (non-marching) passive scalar results show a qualitatively different amount of product when the reactants are switched between the two sides of the layer (this result is very similar to the KD finding). The product thicknesses based on the 'calculated' curves are $\delta_{P1}/\delta = 0.302$ ($\phi = 16$), and $\delta_{P2}/\delta = 0.236$ ($\phi = 16$), (as before, these values are the normalized area under each curve). Comparison of these values to the respective values in table 3 shows one of the deficiencies of the passive scalar method: namely, a factor of 2 overprediction. The matter becomes much worse when the two higher Rx/λ cases are considered. Here, each of the two ϕ- curves have almost the same area under each profile: in figure 18(*b*) the calculated (passive scalar) product thicknesses are $\delta_{P1}/\delta = 0.354$ and $\delta_{P2}/\delta = 0.342$, whereas, in figure 18(*c*), $\delta_{P1}/\delta = 0.345$ and $\delta_{P2}/\delta = 0.325$. In these fully developed cases, the ('marching') passive scalar p.d.f. is unable to capture, even qualitatively, the composition asymmetry.

Next, the mixed-fluid probability $P_m(y)$ is compared for the two experimental techniques (figure 19), for each case. Again, it is seen that the passive scalar results (and especially for the two more fully developed layers) overpredict the amount of mixed fluid. The chemical-reaction data shows that the probability of finding pure unmixed fluid in the centre of the layer, in the asymptotic state, is in the range of 30–40%.

Finally, the averaged mixed-fluid concentration $C_m(y)$ profiles are compared in figure 20 for the three layers. The passive scalar curves show a large lateral variation which is solely the result of poor resolution. For the less developed layer ($Rx/\lambda = 18$), the passive scalar technique again appears to be in less error than for the two more developed layers.

Based upon the comparisons shown in figure 18(*b*, *c*) and figures 20(*b*, *c*) it is clear that the marching p.d.f. is unable to capture the asymmetric entrainment and the correct trends of the mixed mean, and so is incapable of describing the true p.d.f. of the mixing layers studied here; thus it can be eliminated as a descriptor of the asymptotic p.d.f. shape. On the other hand, the non-marching p.d.f. has been shown to represent well the flow at conditions just past the mixing transition based on the

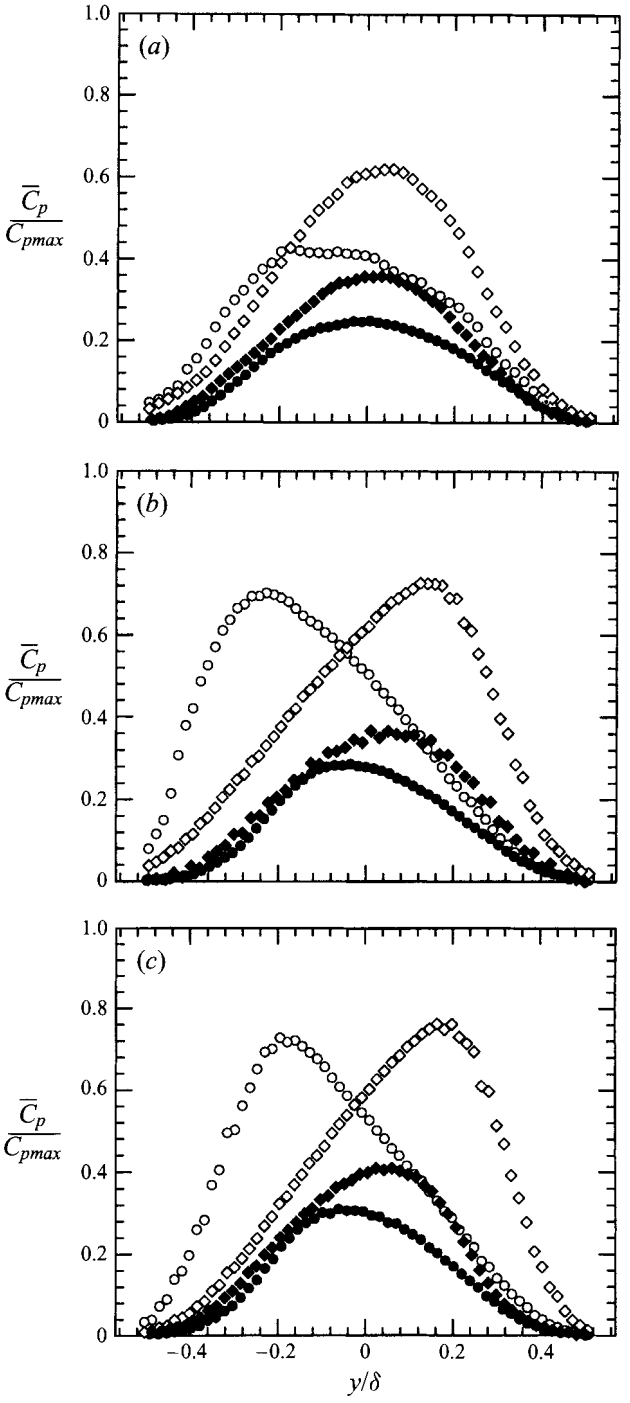

FIGURE 18. Comparison of measured and calculated (from the passive scalar p.d.f.) average product concentration profiles. (*a*) $Rx/\lambda = 18$, (*b*) $Rx/\lambda = 30$, (*c*) $Rx/\lambda = 42$. ○, calculated $\phi = \frac{1}{16}$; ◇, calculated $\phi = 16$; ●, measured $\phi = \frac{1}{16}$; ◆, measured $\phi = 16$.

uniformity of $C_m(y)$ (see figures 17, 18*a*, 20*a* and KD), and the present chemically reacting results show that the flow evolves from symmetric to asymmetric product profiles as the layer becomes more fully developed. These observations can be reconciled by claiming that the asymptotic form of the p.d.f. must be of the tilted type,

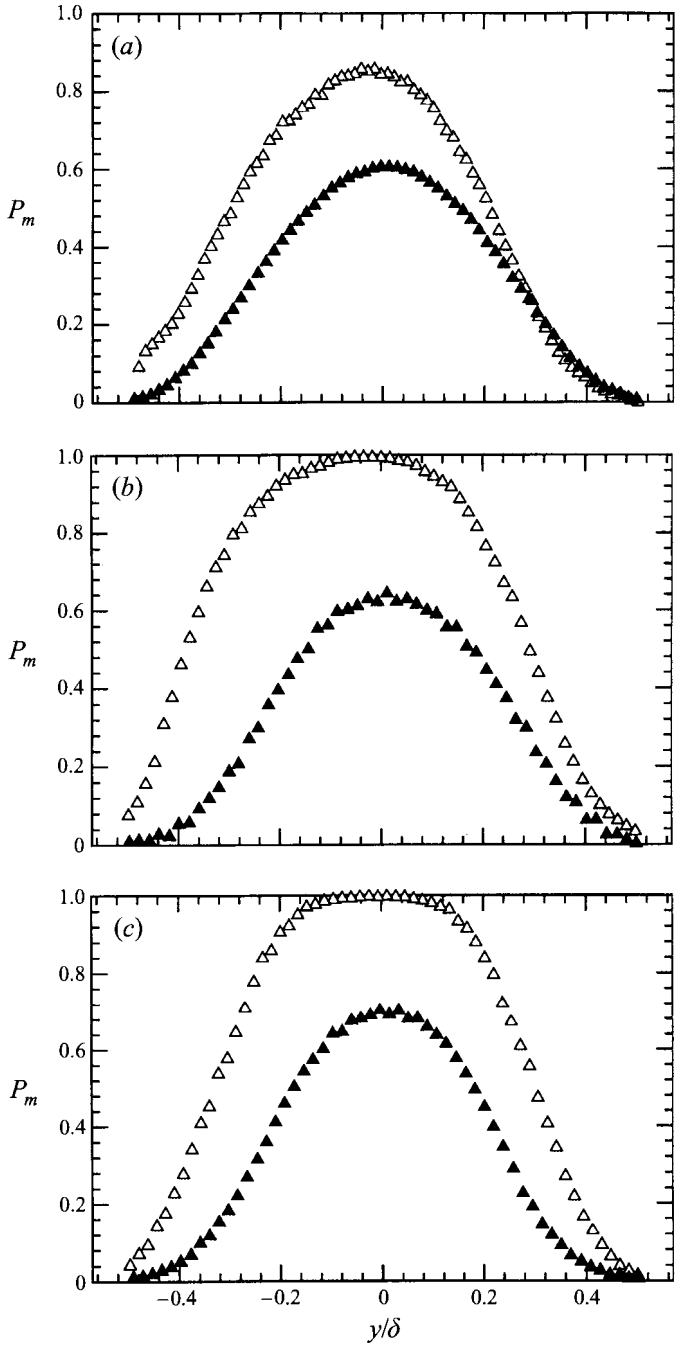

FIGURE 19. Comparison of mixed-fluid probability profiles from △, passive-scalar and ▲, chemical-reaction data. (*a*) $Rx/\lambda = 18$, (*b*) $Rx/\lambda = 30$, (*c*) $Rx/\lambda = 42$.

figure 1(*c*). Such a description would allow entrainment asymmetry, asymmetric product profiles and small variations in the mixed mean as observed here. Thus we conclude that the true p.d.f. evolves from a non-marching character just past the mixing transition to a tilted character in its asymptotic form. It should also be noted that this result holds in spite of the layer appearing disorganized roughly half the time

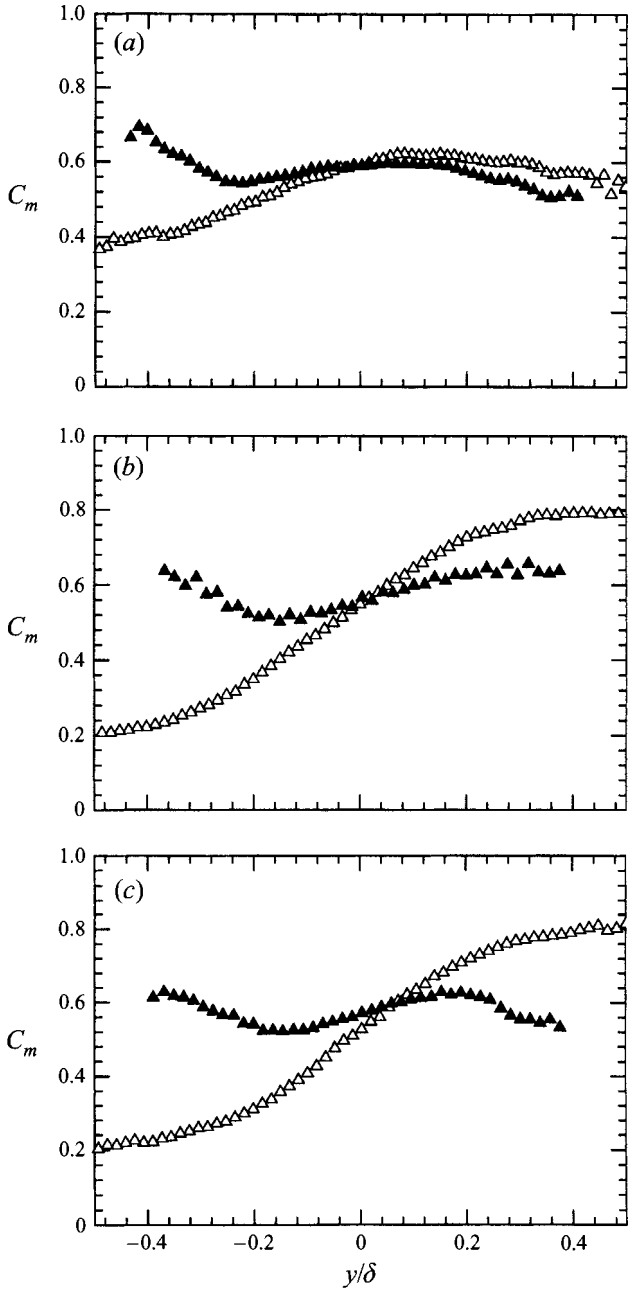

FIGURE 20. Comparison of average mixed-fluid concentration from △, passive-scalar and ▲, chemical-reaction data (*a*) $Rx/\lambda = 18$, (*b*) $Rx/\lambda = 30$, (*c*) $Rx/\lambda = 42$.

(table 2). At this point we wish to mention that our conclusions are in direct contrast to the analyses by Pope (1981) and by Kollmann & Janicka (1982), which produced marching-type p.d.f.s as the asymptotic result.

6.2. *The pairing parameter*

Earlier, Bradshaw (1966) and Breidenthal (1978) had both used x/θ, to define the far field and mixing transition, respectively. However, Huang & Ho (1990) showed that the

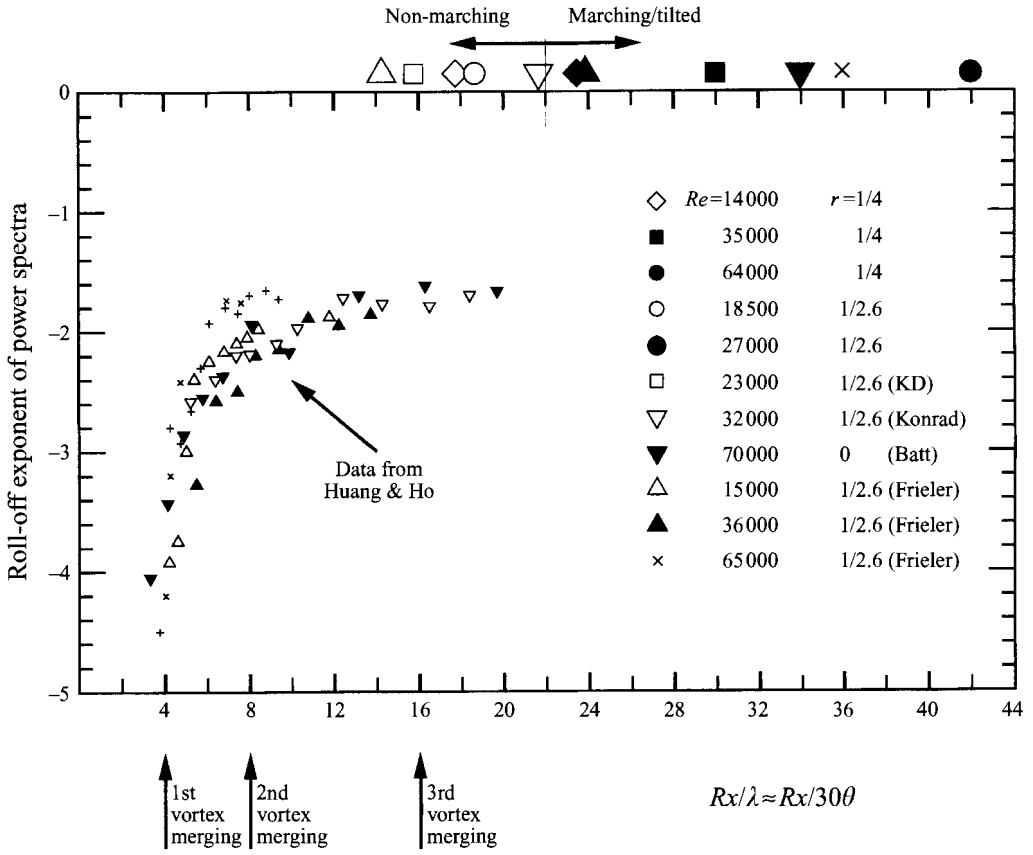

FIGURE 21. Mixture fraction p.d.f. shape *vs.* pairing parameter $Rx/30\theta$. The data are placed above in relation to the plot containing the hydrodynamic measurements of Huang & Ho (1990).

production of small-scale eddies in a plane shear layer, depends on the interaction of large-scale vortical structures. They used the non-dimensional parameter Rx/λ to plot the evolution of the roll-off exponent of the velocity power spectra, n, from the origin to the (hydrodynamic) self-similar region of shear layers (where $R = (1-r)/(1+r)$, x is the downstream distance, and λ is the initial instability wavelength). Their plot is reproduced in figure 21 (for now, consider only the cluster of points labelled as 'data from Huang & Ho'). Furthermore, they found that the position of the first, second, and third large-scale structures' pairings (called mergings in figure 21), which eventually lead to transition and to the fully-developed regime, correlates well with the above parameter for the different layers that they studied. We shall refer to Rx/λ as the 'pairing parameter'.

The pairing-parameter value is then calculated for all untripped cases of the present experiment (passive scalar and chemically reacting), as well as for all other results available in the literature where the p.d.f. was measured or inferred. These include the (only available) liquid-phase layer by KD, and the gaseous-phase layers of Batt (1977), Konrad (1976), and Frieler (1992). In doing so, λ was estimated through the relation $\lambda \approx 30\theta$ established by various studies (Monkewitz & Huerre 1982; Huang & Ho 1990), where θ is the initial high-speed boundary-layer momentum thickness. For our own cases, we verified that the above relation gives a good estimate by performing close-up visualizations of the flow region just past the splitter plate tip, and measuring

the wavelength λ of the first wave. The $\lambda \approx 30\theta$ relation was found to be accurate to within $\pm 9\%$ for all cases (except for the $r = \frac{1}{4}$, $Re = 64000$ case, for which it was off by about -20% from the measured first wavelength). For the KD case, the data given in Breidenthal (1978) was used to estimate θ (same facility used by KD). For the Batt layer, θ was easily calculated from Batt's own measurements in the boundary layer (Batt 1975). The θ value for Konrad's case has the largest ambiguity, as it was estimated (using Thwaites' method) by inferring the geometry of the facility through a photograph (Brown & Roshko 1974, plate 1) and through quoted geometrical dimensions. Finally, Frieler (three different layers) gives detailed estimates of the value of θ. The results for θ and the estimated pairing parameter, $Rx/30\theta$, appear in table 1.

From this table we notice that, all layers for which the corresponding pairing parameter is less than about 22 have a non-marching p.d.f., whereas layers for which the pairing parameter is about 22 have marching p.d.f.s if measured by the passive scalar technique, including the results of Batt. If one considers only the more reliable chemical reaction results, then the revised observation is that the p.d.f. is non-marching for a pairing parameter below 22 (KD, Frieler, present $Rx/\lambda = 18$) and tilted for values above (Frieler $Rx/\lambda = 24$, 36 and present $Rx/\lambda = 30$, 42). To further illustrate this state, in connection with the data of Huang & Ho, we mark on the top margin of figure 21 all examined cases (only untripped layers are considered) according to their corresponding $Rx/30\theta$ value. An important observation is that experiments with similar Re numbers may differ significantly in their $Rx/30\theta$ value as a result of different operating conditions imposing different initial conditions. Thus, in terms of the shape of the p.d.f.s under consideration, it seems that the Reynolds number alone is not sufficient to characterize the scalar field. The mixing transition, whereby the amount of molecularly mixed fluid suddenly increases, is now logically associated with the locations past the second vortex merging. Beyond this region though, the scalar field appears to continue to evolve, and yields an asymptotic state at locations well past the third vortex merging. The evolution to this new state is not a function of the Reynolds number, but of the non-dimensionalized distance Rx/λ, at which sufficiently energetic vortices merge to produce small-scale eddies.

Figure 21 also suggests that the layer achieves its hydrodynamic fully-developed state before achieving its scalar fully-developed state, since the velocity-spectra exponent reaches an asymptotic value at $Rx/\lambda \approx 16$. On the other hand, the exact location of the third vortex merging most probably depends upon the particular experiment, and is not necessarily 'fixed' at the value of 16 (see also the work of Ho *et al.* 1991). Also, and as Huang & Ho pointed out, the Reynolds number must be high enough to allow the cascade to the smallest scales. Our measurements, combined with those of Huang & Ho, indicate that 'transition' to the fully-developed state is tied to the number of vortex pairings. This explains why the comparison between our results and the results by KD should not be based on the Reynolds number alone. Furthermore the exact value of the pairing-parameter threshold for a change in the p.d.f.-shape is probably variable, and depends on parameters such as the Schmidt number, the free-stream turbulence level, the energy content of the initial laminar boundary layers, which the experimentalist cannot easily simultaneously document or systematically vary in a given study. We believe though, that by performing a set of experiments in the same facility, some of the 'unknown parameters' that influence the mixing layer are reduced, and reliable conclusions can be reached. In particular, with respect to the effect of the initial boundary layers, the reader is encouraged to consult the DNS results of Rogers & Moser (1994), where they show that the degree of

amplification that is imposed on the initial turbulent boundary layers determines whether marching or non-marching p.d.f.s are obtained; we shall return to this result later. Our main point however, is that the *Re* alone is inadequate for characterizing the scalar field of mixing layers, and a parameter which also takes into account the initial conditions should be considered instead. To the extent of the latest available data, we propose that this parameter be Rx/λ.

Figure 21 now places the results of Batt (1977) in context. His resolution is only three times worse than Konrad's, (and very much better than KD) but his (passive scalar) p.d.f. is found to be marching. In terms of the present findings, his pairing parameter is about 34, while Konrad was just under 22, so that the Batt results fall into the 'marching' regime. In the content of the present results, we would conclude that his measured p.d.f. is erroneous and since working in gas, his true p.d.f. is actually closer in character to the type measured by Frieler, namely a tilted p.d.f., with U-shaped functions as depicted in figure 1(*c*).

Concerning tripping, there are two observations. The first arises from comparison of the $r = \frac{1}{2.65}$, $Re = 18\,500$ case with its tripped counterpart. The untripped case shows a non-marching behaviour, with some break-away towards the low-speed side. Tripping turns this p.d.f. into marching. The second observation is based on the comparison between untripped and tripped cases for the $r = \frac{1}{4}$ layers. It is seen first, that once the layer achieves a state characterized by marching p.d.f.s ($Re = 14\,000$ and $Re = 35\,000$), tripping does not affect the overall (qualitative) shape of the passive scalar p.d.f. Furthermore, the $Re = 14\,000$ case remained non-marching upon tripping. The fact that tripping in these latter cases did not affect the qualitative shape of the p.d.f. does not, by any means, suggest that tripping does not cause changes in the flow: remember that tripped layers exhibited diminished growth rates. Based on our (limited) passive scalar results, it seems that tripping, as suggested by Bell & Mehta (1990) for the velocity field, will also cause the scalar field to move towards a direction closer to a far-field, asymptotic state.

6.3. *Gas–liquid differences and other comparisons*

The present liquid-phase results were compared earlier to the gaseous-phase results obtained by Mungal & Dimotakis (1984), Mungal *et al.* (1985), and Frieler (1992). All three gaseous-phase investigations were performed in the same facility, using an H_2/F_2 chemical reaction.

Frieler did not measure directly the mixture fraction p.d.f., but mathematically constructed it to fit his available chemical-product data. However, chemical data are (on average) free from resolution limitations, and the Frieler p.d.f.s are thus likely to be correct. His three cases are listed in table 1. His $Rx/30\theta = 14$ case is non-marching, while his two cases $Rx/30\theta > 22$ are tilted. His results, along with the present findings, strongly suggest that, at conditions past the mixing transition, the layer is changing as the flow becomes more fully developed, and hence his results were plotted in figure 21. We note that Mungal (1983) had earlier obtained tilted p.d.f.s similar to that of Frieler for chemically reacting experiments in the same facility at run conditions similar to those of Frieler. Mungal inverted his product profiles to produce a p.d.f. represented by seven delta functions at each of eight locations across the layer, and obtained a tilted p.d.f. (see his figure 34); however, the Frieler work is much more extensive in this regard and is taken to be the definitive result on the p.d.f. at high values of pairing parameter for gaseous layers.

For comparison of gas–liquid differences, first the product thickness (volume-fraction of chemical product) is compared for each case, as it is a measure of the layer's

mixing efficiency. The comparisons are shown in figure 11 for the low-ϕ and the high-ϕ limit. Only matched free-stream density layers are considered. The plots show that the amount of product differs significantly between gases and liquids, for all conditions examined. This result was reported earlier by KD; however, as shown before, their layer was not fully developed. The present study allows us to assess the behaviour of liquids for fully developed conditions. Figure 11 (*a*) indicates that the mixing efficiency of the liquid layer is almost uniform (or, shows a very slight increasing tendency) as more fully-developed conditions are reached. Gases show the opposite behaviour. The high-ϕ data, figure 11 (*b*), shows constant product thicknesses for both gaseous- and liquid-phase layers.

Next, the average concentration of mixed fluid $C_m(y)$ is considered. Figure 13 shows the corresponding profiles for liquid and gas. The much stronger variation across the gaseous curve of Mungal, indicates that molecular diffusion has a significant effect, throughout the experimentally examined conditions. It thus becomes imperative to incorporate this Schmidt-number dependency in models and calculations of scalar mixing in any turbulent flow.

We next discuss our findings in the context of the Broadwell–Breidenthal (B–B) model which envisages the product as residing in either 'homogeneous' regions or 'flame sheet' regions and allows for explicit gas–liquid differences. The B–B model predicts that the amount of product which is formed in the homogeneous part of the layer is independent of *Re* and *Sc*, and is a function of the entrainment ratio (for stoichiometric ratios larger than the entrainment ratio). On the other hand, the product formed in the flame sheet is dictated by diffusion-limited reactions. In the p.d.f., the flame sheet is represented by the U-shape functions (dotted curves) shown schematically in figure 1. The characteristic scale of the flame sheet, $\delta_{f.s.}$, is determined from diffusion-flame theory to be $\delta_{\mathrm{f.s.}}/\delta \sim 1/(Re\,Sc)^{\frac{1}{2}}$. The ratio of the amount of product in the flame sheet to the amount of product in the homogeneous part is not modelled, and therefore must be determined through experiments. The model predicts that the contribution of the flame sheet into the total product is negligible in liquids ($Sc \gg 1$) compared to that in gases, and that the amount of product in a liquid layer should be almost constant as the layer becomes more developed. Our data supports these aspects of the B–B model. However, the present study has shown that the liquid layer evolves as it goes from conditions just past the mixing transition (KD layer) to the most fully developed conditions examined: the results showed that $C_m(y)$ develops a small lateral variation (slope) as *Re* increases. Within the frame of the B–B model, there are two possible ways to explain this evolution. The first explanation assumes that a finite amount of product, albeit very small, resides in the flame sheet of the liquid layer. Our measurements then suggest that when *Re* is increased, a somewhat larger percentage of the total chemical product resides in the flame sheet (δ_{fs}/δ_P increases), which, as in the case of gases, results in a local biasing of the average mixed-fluid composition. In this case the fully-developed liquid p.d.f. can be thought to be of the non-marching type, but with a small enhancement (relative to the KD p.d.f.) of the U-shape functions. The second explanation assumes that the flame-sheet contribution is indeed negligible in liquids. The observed variation in $C_m(y)$ can then be explained as a result of 'local homogenization' in the layer. In this second case, the p.d.f. would have a tilted shape for the mean mixed-fluid composition; this is the description which has been used throughout this work, as the B–B model by nature of its simplicity assumes that the liquid flame-sheet contribution is zero.

The Dimotakis (1989) model remains supported by our results to the extent that our liquid product measurements are in agreement with KD. In this model the amount of

mixed fluid is constructed from an ensemble of strained diffusion flames whose thicknesses scale with the diffusivity of the medium (gas or liquid). While no p.d.f.s are shown, the model computes the total amounts of product formed between chemical reactions occurring in gases or liquids. Finally, we wish to leave the reader with the notion that, although some of the fine details of the p.d.f. are still debatable, it is clear that in no way does a marching p.d.f. characterize any of the layers examined in this work.

Rogers & Moser (1994) were able to find both non-marching as well as marching p.d.f.s, at Re up to 20000 dependent upon the nature of forcing of a mixing layer which grows from initially turbulent boundary layers. More significant, however, is the fact that their layer grows by only about ten times its initial momentum thickness during the course of the computation. In contrast to this, a pairing parameter of $Rx/30\theta = 20$ translates into $\delta/\theta = 20 \times 30 \times C \approx 200$, since $\delta/x = CR$ and $C \approx \frac{1}{3}$ (table 2), i.e. the present experimental layer grows to about 200 times its initial thickness at the fully developed condition. Thus, it appears that the numerical layer may be more closely related to its initial conditions after having grown by only ten times its initial thickness, in spite of the Re achieved.

We also note that the present data do not allow predictions to be made in the limit of 'very high' values of Rx/λ or, equivalently, in the limit of 'very high' Reynolds numbers. The fitted curves (straight lines) in figure 11 cannot reveal any asymptotic trend. The fitted lines for gas and liquid, would actually intersect at Rx/λ values of about 130 (sixth pairing) and 400 (past seventh pairing) for the low-ϕ and the high-ϕ case, respectively, where the Reynolds number was estimated to be in the range of 10^6 to 10^7. However, there is no evidence that this straight-line fit is correct, or that each line will not level off to some asymptotic value before intersecting. Thus, the quest to identify the 'ultimate' fully developed state of turbulent mixing is not yet over.

6.4. *Reconciliation of passive scalar with chemical reaction measurements*

The present chemical reaction findings argue for a p.d.f. which evolves from a non-marching to tilted behaviour past the third pairing. At the same time, the passive scalar results incorrectly suggested a non-marching to marching behaviour. Given the strict resolution requirements for the passive scalar to be accurate and the fact that we were unable to artificially cause the non-marching p.d.f. to march, one might question why the passive scalar approach ever produced a non-marching p.d.f. at all. Here, we will use these observations to infer the types of physical changes that are likely to be occurring in the flow. Figure 22 shows a series of sketches representing a pixel on the camera and the types of scalar distributions that might be seen; the shading is used to denote concentration. Each row is a representation of the actual scalar field (left-hand box) and the inferred scalar field as measured by the passive scalar technique (middle box) and by the chemical reaction technique (right-hand box). Box 1 illustrates a distribution of pure free-stream fluids, represented by black ($\xi = 0$) and mostly white ($\xi = 1$) shading, within the measurement volume with a small amount of actual mixing on the interface. Box 2 shows that this will be reported the passive scalar measurement as mixed fluid, nearly white in composition ($\xi \approx 1$), while Box 3 shows that the chemical reaction technique will correctly report a small amount of reaction and thus mixing. This top row is a model of the scalar field for the low pairing parameter cases ($Rx/\lambda < 22$) and would lead to non-marching p.d.f.s that are qualitatively correct but which overpredict the actual, symmetric chemical product profiles. Comparing with figure 14(*a*), such a model would allow significant r.m.s. variations from pixel to pixel as revealed in the spanwise and streamwise cuts.

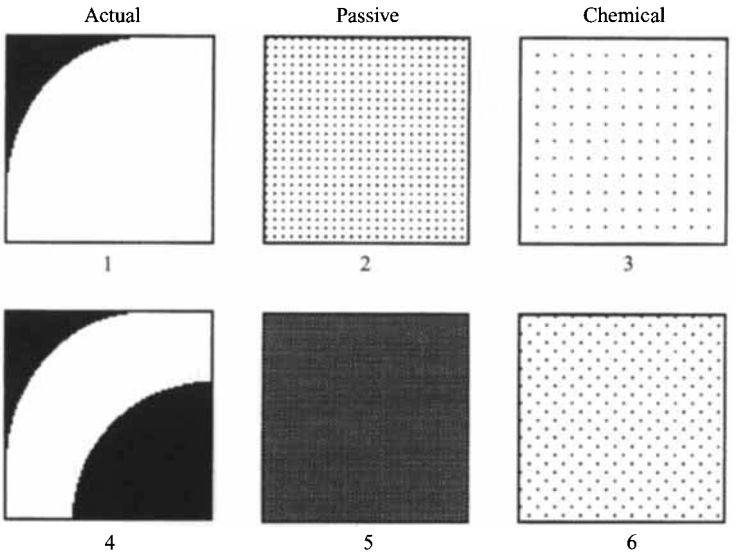

FIGURE 22. Schematic illustration of scalar distribution withing a pixel and result recorded by passive scalar and chemical reaction approaches. Model for low Rx/λ (upper) and high Rx/λ (lower).

The lower row of figure 22 is proposed as a type of change occurring in the flow under high pairing parameter cases ($Rx/\lambda > 22$). Here a scalar distribution in the flow at subpixel dimensions as shown in Box 4 will lead to a small increase in chemical product (Box 6) and thus correct mixing, but with a large increase in passive-scalar-inferred mixing (Box 5), which is incorrect. Comparing now with figure 14(*e*) we see much less variation from pixel to pixel as revealed by the smaller r.m.s. variations in the spanwise and streamwise cuts. While this model is not expected to be accurate in details, it illustrates the nature of changes than can occur at sub-pixel dimensions leading to the observed changes in the passive scalar and chemical reaction results. In particular, we believe that these subpixel changes only manifest themselves past the third pairing, at which point the scalar field achieves its asymptotic state.

7. Conclusions

The present liquid-layer experiments are considered to be a confirmation and extension of the work by Koochesfahani & Dimotakis (1986). For operating conditions which are just past the mixing transition, the present study has essentially duplicated all the results obtained by KD. However, when the layer was examined at more fully developed conditions, changes in the scalar field were discovered. These changes are depicted in figure 10, where it is seen that, the flip chemical-product profiles are initially symmetric (figure 10*a*), but they develop a small asymmetry when more fully developed conditions are reached (figure 10*b*, *c*). This asymmetry in the chemical-product is suggestive of a mild departure from homogeneous mixing across the entire layer at a single composition. The mixed-fluid composition is presented in figure 13, and confirms that the fully developed layers ($Rx/\lambda = 30$, $Rx/\lambda = 42$) carry a small lateral variation in the average mixed-fluid concentration when compared to the more uniform profiles of the less developed $Rx/\lambda = 16$ and KD layers. The observed variation of $C_m(y)$ is different from the large lateral gradient obtained in gaseous layers, so that the differences associated with Schmidt number persist in the asymptotic limit. Thus, the

present study validates some of the basic aspects of the Broadwell–Breidenthal model, and also the Dimotakis model. Despite the changes in the $C_m(y)$ profiles, the total mixed-fluid average concentration (C_M) was found to be constant at about 0.58 (table 3). The present measurements indicate that, for the liquid layer, the total (integrated across the entire layer) volume-fraction of mixed fluid increases slightly as more fully-developed conditions are reached. The entrainment asymmetry, already documented by KD, was seen to exist for all flow regimes and results in different amounts of product formed in the flip experiments. Finally, our findings show that the results obtained by Koochesfahani & Dimotakis and by Konrad are not fully representative of far-field conditions. We believe that the most developed case studied, is close to representing the asymptotic liquid layer, supported by the fact that C_M remained constant, and by the similarity in the $C_m(y)$ curves for the two most developed cases.

In the present work in addition to the chemical-reaction technique, a passive-scalar technique was used to probe the layer. The results showed that the passive scalar measurements with associated spatial resolution inadequacies, lead to erroneous results. However, the passive scalar p.d.f. revealed that changes in the p.d.f. were congruent to the (true) changes depicted by the resolution-free, chemical-reaction data at identical operating conditions. Based on these changes, we showed that the Reynolds number alone is inadequate for characterizing the scalar field in shear layers. Instead, the pairing parameter, Rx/λ, was found to explain adequately the evolution of the scalar field. The pairing parameter includes the effects of initial conditions which are known to affect the state of the layer, and incorporates all speed ratios. Our results suggest that the second pairing is associated with the mixing transition, while going past the third pairing is required for fully developed conditions in the scalar field; equivalently this corresponds to the layer width having grown to over 200 times its initial momentum thickness. By comparison to velocity measurements, it appears that the velocity field becomes asymptotic before the scalar field. Finally, since the resolution-free chemical-reaction data produced a very small lateral variation of $C_m(y)$ at far-field conditions, this implies that the true p.d.f. evolves from a non-marching to a tilted behaviour in the asymptotic limit in contrast to the passive scalar p.d.f. evolving from an initial qualitatively-correct non-marching p.d.f. to a final, incorrect marching p.d.f. It is argued that changes at subpixel dimensions (figure 22) are responsible for the incorrect passive scalar results, and that this effect worsens as the flows evolves; in particular, the data of Batt would have suffered from this effect. By comparison to the chemically reacting results, under no conditions do we conclude that the marching p.d.f. serves as a good representation of the observed scalar mixing field (figures 18–20) and is in contrast to the findings of Rogers & Moser. These conclusions are notwithstanding the fact that the layer lacks obvious organization about 50% of the time (table 2).

To discount some of the unknown parameters that influence the development of shear layers, most of the results were normalized by the layer's average width. The issue of growth rate was explored by measuring layers starting from untripped and tripped initial boundary layers. The results showed that tripped layers have a growth rate diminished by 10% to 25%. Furthermore, the layer's growth rate was seen to decrease as the free-stream velocity magnitudes were increased. Passive scalar measurements suggested that tripping makes the layer achieve far-field characteristics at an earlier downstream distance.

The authors wish to thank Dr J. M. Seitzman for his generous help, and Professor R. K. Hanson for the use of the Pixar Imaging System. We also thank J. E. Broadwell

and M. M. Koochesfahani for helpful discussions of the results. This work was supported by the Stanford-Ames Center for Turbulence Research, and by the NSF (contract no. CTS-9020641).

REFERENCES

BATT, R. G. 1975 Some measurements on the effect of tripping the two-dimensional shear layer. *AIAA J.* **13**, 245.

BATT, R. G. 1977 Turbulent mixing of passive and chemically reacting species in a low-speed shear layer. *J. Fluid Mech.* **82**, 499.

BELL, J. H. & MEHTA, R. D. 1990 Development of a two-stream mixing layer from tripped and untripped boundary layers. *AIAA J.* **28**, 2034.

BERNAL, L. P. & ROSHKO, A. 1986 Streamwise vortex structure in plane mixing layers. *J. Fluid Mech.* **170**, 499.

BRADSHAW, P. 1966 The effects of initial conditions on the development of a free shear layer. *J. Fluid Mech.* **26**, 225.

BREIDENTHAL, R. E. 1978 A chemically reacting turbulent shear layer. PhD thesis, Caltech.

BREIDENTHAL, R. E. 1981 Structure in turbulent mixing layers and wakes using chemical reaction. *J. Fluid Mech.* **109**, 1.

BROADWELL, J. E. & BREIDENTHAL, R. E. 1982 A simple model of mixing and chemical reaction in a turbulent mixing layer. *J. Fluid Mech.* **125**, 397.

BROWAND, F. K. & LATIGO, B. O. 1979 Growth of the two-dimensional mixing layer from a turbulent and non-turbulent boundary layer. *Phys. Fluids* A **22**, 1011.

BROWAND, F. K. & TROUTT, T. R. 1980 A note on spanwise structure in the two-dimensional mixing layer. *J. Fluid Mech.* **97**, 771.

BROWN, G. L. & ROSHKO, A. 1974 On density effects and large structure in turbulent mixing layers. *J. Fluid Mech.* **64**, 775.

CLEMENS, N. T. & MUNGAL, M. G. 1992 Two- and three-dimensional effects in the supersonic mixing layer. *AIAA J.* **30**, 973.

CLEMENS, N. T. & MUNGAL, M. G. 1995 Large-scale structure and entrainment in the supersonic mixing layer. *J. Fluid Mech.* **284**, 171.

CLEMENS, N. T. & PAUL, P. H. 1995 Scalar measurements in compressible axisymmetric mixing layers. *Phys. Fluids* 7(5), 1071.

DIMOTAKIS, P. E. 1986 Two-dimensional shear layer entrainment. *AIAA J.* **24**, 1791.

DIMOTAKIS, P. E. 1989 Turbulent shear layer mixing with fast chemical reactions. In *Turbulent Reacting Flows* (ed. R. Borghi & N. B. Murthy). Lectures Notes in Engineering, vol. 40, p. 417. Springer.

DIMOTAKIS, P. E. 1991 Turbulent free shear layer mixing and combustion. High Speed Flight Propulsion Systems. *Prog. Astronaut. Aeronaut.* **137**, 265.

DIMOTAKIS, P. E. & BROWN, G. L. 1976 The mixing layer at high Reynolds number: large-structure dynamics and entrainment. *J. Fluid Mech.* **78**, 535.

FRIELER, C. E. 1992 Mixing and reaction in the subsonic two-dimensional turbulent free shear layer. PhD thesis, Caltech.

HANSON, R. K. 1986 Planar imaging techniques. *21st Intl Symp. Combust.*, p. 1677. The Combustion Institute.

HO, C.-M., ZOHAR, Y., FOSS, J. K. & BUELL, J. C. 1991 Phase decorrelation of coherent structures in a free shear layer. *J. Fluid Mech.* **230**, 319.

HUANG, L.-S. & HO, C.-M. 1990 Small scale transition in a plane mixing layer. *J. Fluid Mech.* **210**, 475.

HUSSAIN, A. K. M. F. & CLARK, A. R. 1981 On the coherent structure of the axisymmetric mixing layer: a flow visualization study. *J. Fluid Mech.* **104**, 263.

JIMENEZ, J., COGOLLOS, M. & BERNAL, L. P. 1985 A perspective view of the plane mixing layer. *J. Fluid Mech.* **152**, 125.

KARASSO, P. S. 1994 Experiments on mixing and reaction in plane and curved turbulent shear layers. PhD thesis, Stanford University.

KARASSO, P. S. & MUNGAL, M. G. 1990 An experimental study of curved mixing layers: flow visualizations using volume rendering. Center for Turbulence Research Annual Briefs, Stanford.

KARASSO, P. S. & MUNGAL, M. G. 1992 LIF measurements of mixing in turbulent shear layers. *Sixth Intl Symp. on Applications of Laser Techniques to Fluid Mechanics*, Lisbon, Portugal.

KARASSO, P. S. & MUNGAL, M. G. 1996 PLIF measurements in aqueous flows using the Nd:YAG laser. *Expts. Fluids* (submitted).

KOLLMANN, W. & JANICKA, J. 1982 The probability density function of a passive scalar in turbulent shear flows. *Phys. Fluids* **25**, 1755.

KONRAD, J. H. 1976 An experimental investigation of mixing in two-dimensional turbulent shear flows with applications to diffusion-limited chemical reactions. PhD thesis, Caltech.

KOOCHESFAHANI, M. M. 1984 Experiments on turbulent mixing and chemical reactions in a liquid mixing layer. PhD thesis, Caltech.

KOOCHESFAHANI, M. M. & DIMOTAKIS, P. E. 1986 Mixing and chemical reactions in a turbulent liquid mixing layer. *J. Fluid Mech.* **170**, 83.

KYCHAKOFF, G., HOWE, R. D. & HANSON, R. K. 1984 Quantitative flow visualization technique for measurements in combustion gases. *Appl. Optics* **23**, 704.

MONKEWITZ, P. A. & HUERRE, P. 1982 The influence of the velocity ratio on the spatial instability of mixing layers. *Phys. Fluids* A **25**, 1137.

MUNGAL, M. G. 1983 Experiments on mixing and combustion with low heat release in a turbulent shear flow. PhD thesis, Caltech.

MUNGAL, M. G. & DIMOTAKIS, P. E. 1984 Mixing and combustion with low heat release in a turbulent mixing layer. *J. Fluid Mech.* **148**, 349.

MUNGAL, M. G., HERMANSON, J. C. & DIMOTAKIS, P. E. 1985 Reynolds number effects on mixing and combustion in a reacting shear layer. *AIAA J.* **23**, 1418.

POPE, S. B. 1981 A Monte-Carlo method for the PDF equations of turbulent reactive flows. *Combust. Sci. Tech.* **25**, 159.

ROGERS, M. M. & MOSER, R. D. 1994 Direct simulation of a self-similar turbulent mixing layer. *Phys. Fluids* A **6**, 903.

WARE, B. R., CYR, D., GORTI, S. & LANNI, F. 1983 *Measurements of Suspended Particles by Quasi-Elastic Light Scattering*. Wiley.

WINANT, C. D. & BROWAND, F. K. 1974 Vortex pairing: the mechanism of turbulent mixing layer growth at moderate Reynolds number. *J. Fluid Mech.* **63**, 237.

WOOD, D. H. & BRADSHAW, P. 1982 A turbulent mixing layer constrained by a solid surface. Part 1. Measurements before reaching the surface. *J. Fluid Mech.* **122**, 57.